

RESULTS AND DISCUSSION

1. Part I: SUZ-4 Zeolite Synthesis

From experiment conditions, several Al^{3+} and Si^{4+} sources were used to produce SUZ-4. It was found that the absence or near absence of Na^+ in the gel composition is important for SUZ-4 crystallization in TEA^+ system. Na^+ cation inhibited the formation of SUZ-4. This result is consistent with the previous works (Asensi *et al.*, 1999; Price, 2001). Moreover, the chemical compositions, crystallization of temperature, time and rotation of autoclaves were key factors for this new SUZ-4 zeolite synthesis. To study the parameters for synthesis, the results of SUZ-4 synthesis using aluminum powder and Ludox AS-40 in both types of reactors were interpreted. Crystallization of SUZ-4 powder and SUZ-4 membrane were discussed, respectively.

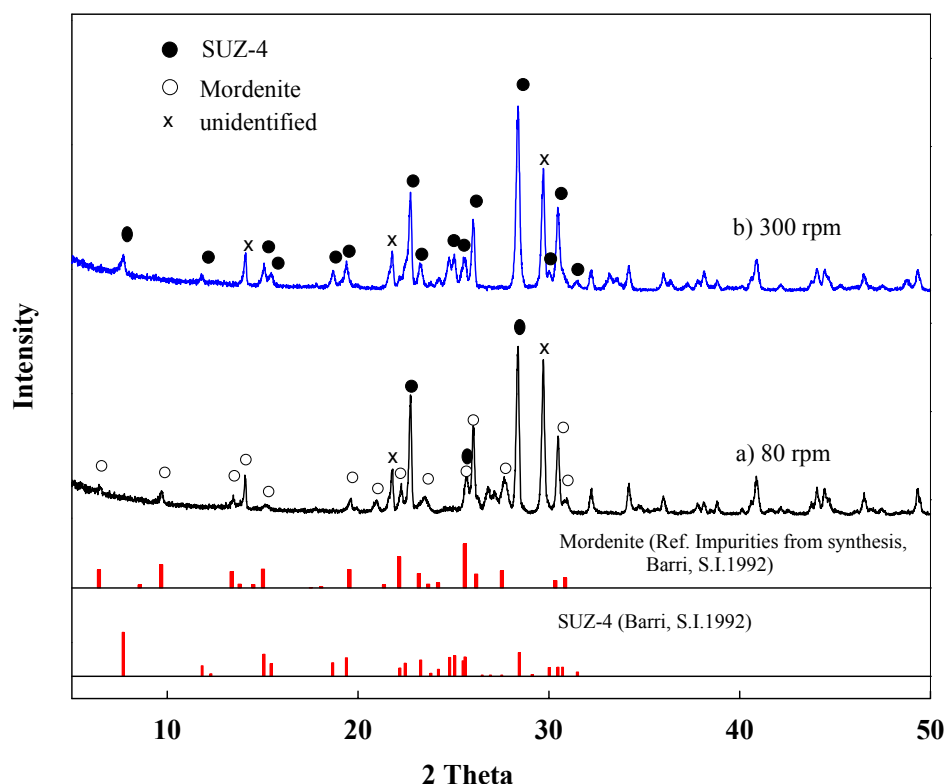
1.1 The Effect of Stirring on the Formation of SUZ-4 Zeolite

The agitation of prepared gel having compositions as shown in Table 7 ($\text{SiO}_2/\text{Al}_2\text{O}_3 = 33$, $\text{TEA}_2\text{O}/\text{Al}_2\text{O}_3 = 3.10$, $\text{H}_2\text{O}/\text{Al}_2\text{O}_3 = 800$, $\text{K}_2\text{O}/\text{Al}_2\text{O}_3 = 7.3$) on base recipes were studied and the product was retrieved after crystallization at 155 °C for 4 days. The results show that the product from slow stirring of the autoclaves (80 rpm) was mainly obtained mordenite (MOR) with unidentified phase and SUZ-4 zeolite in trace. On the other side, when agitation was increased to 300 rpm, SUZ-4 zeolite was mainly obtained with unidentified phase presented in trace amounts. Stirring condition for SUZ-4 synthesis is consistent with the previous studies reported that well-defined SUZ-4 zeolite structure was only obtained under stirring of 250 rpm or more (Kim *et al.*, 2004). Using energy dispersion X-ray analysis (EDS) as shown in Appendix D, it was found to have different Si/Al (by weight) depending on starting $\text{SiO}_2/\text{Al}_2\text{O}_3$.

Table 7 Effect of stirring for 4 days crystallization time at $\text{SiO}_2/\text{Al}_2\text{O}_3 = 33$.

No.	$\text{SiO}_2/\text{Al}_2\text{O}_3$	$\text{TEA}_2\text{O}/\text{Al}_2\text{O}_3$	$\text{H}_2\text{O}/\text{Al}_2\text{O}_3$	$\text{K}_2\text{O}/\text{Al}_2\text{O}_3$	Temp ($^\circ\text{C}$)	Stirring (rpm)	Product	Si/Al
8	33.42	3.10	770.81	7.29	156	80	MOR+unidentified +SUZ-4	n/a
9	33.51	3.09	811.59	7.37	151	300	SUZ-4+unidentified	~12.1
15	32.40	3.05	794.60	7.19	154	300	SUZ-4+unidentified	~6.5

The XRD peaks in Figure 7 reveal that SUZ-4 zeolite was mainly obtained with unidentified phase presented in trace amounts with stirring at 300 rpm comparing with 80 rpm that has competing phase of MOR. The result shows that not only Na^+ cation on chemical preparation affects on SUZ-4 zeolite synthesis, but agitation system is also one of the main factors for this new type of SUZ-4 zeolite.

**Figure 7** XRD patterns of zeolite SUZ-4 crystals prepared at $\text{SiO}_2/\text{Al}_2\text{O}_3 = 33$ for 4 days compared with different stirring speeds (a) 80 rpm (b) 300 rpm.

1.2 The Effect of SiO₂/Al₂O₃ Molar Ratios and Crystallization Time on Characteristic Properties of SUZ-4 Zeolite

For these experiments, the crystallization reaction time was studied with 2 conditions for 4 days and 2 days synthesis. Under stirring at around 300 rpm of autoclaves and 151-155 °C for 4 days crystallization time as shown in Table 8, the recipes were prepared and found that as SiO₂/Al₂O₃ decreased, the TEA₂O/Al₂O₃ and K₂O/Al₂O₃ required forming SUZ-4 also decreased (Asensi *et al.*, 1999; Price, 2001; Kim *et al.*, 2004). It was also observed that the gel mixture with high SiO₂/Al₂O₃ was very viscous and as the ratio decreased, it became less viscous. Mainly SUZ-4 from SiO₂/Al₂O₃ = 21.2 indicated Si/Al (by weight) was 6.7-6.8 using energy dispersion X-ray analysis (EDS).

Table 8 Effect of different SiO₂/Al₂O₃ at stirring around 300 rpm for 4 days crystallization.

No.	SiO ₂ / Al ₂ O ₃	TEA ₂ O/ Al ₂ O ₃	H ₂ O/ Al ₂ O ₃	K ₂ O/ Al ₂ O ₃	Temp (°C)	Product	Si/Al
9	33.51	3.09	811.59	7.37	151	SUZ-4+ unidentified	~12.1
15	32.40	3.05	794.60	7.19	154	SUZ-4+unidentified	~6.5
10	21.24	1.30	500.80	4.00	155	SUZ-4	~6.7
16	21.15	1.30	498.92	3.96	152	SUZ-4	~6.8
11	16.26	0.92	464.10	3.96	155	SUZ-4+ unidentified	~6.1

Figure 8 shows XRD patterns with different SiO₂/Al₂O₃ ratios for 4 days crystallization, using the SiO₂/Al₂O₃ ratios of 32.4 and 16.3 gave unidentified phase as impurity of product. Good sample of synthesized SUZ-4 zeolite for 4 days crystallization time can be produced from gel mixture of SiO₂/Al₂O₃ = 21.2 under experiment conditions. The result reveals that chemical composition of mixture is also very sensitive for SUZ-4 synthesis.

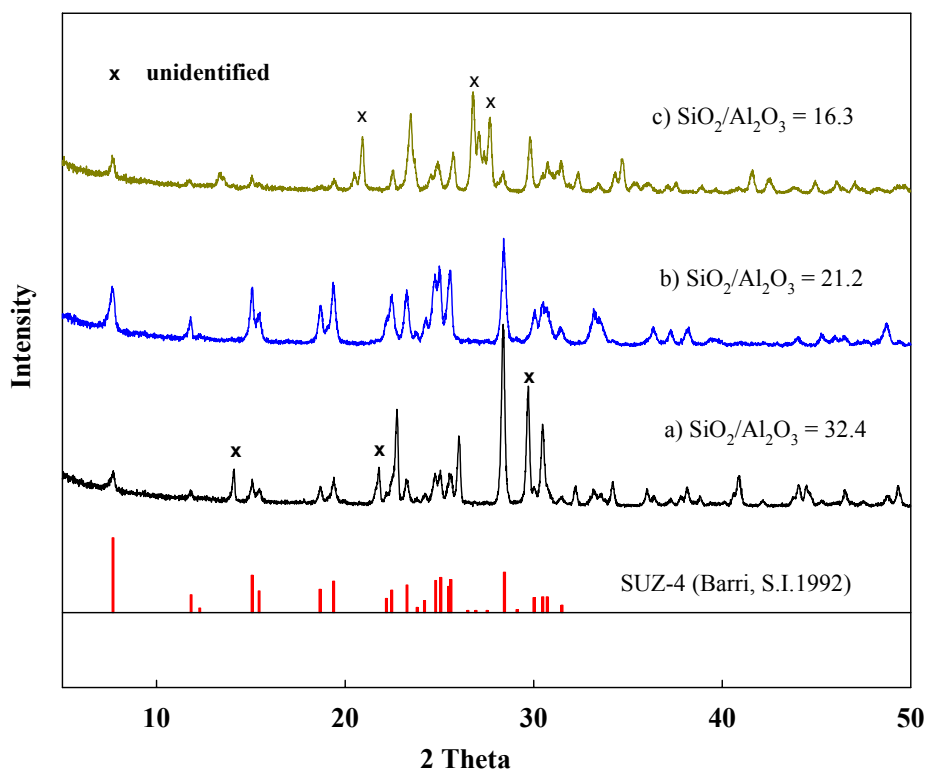


Figure 8 XRD patterns of zeolite SUZ-4 crystals prepared at 155 °C for 4 days with different SiO₂/Al₂O₃ (a) 32.4 (b) 21.2 (c) 16.3.

The SEM images of SUZ-4 zeolite prepared using TEAOH template for 4 days under autogenous pressure are shown in Figure 9. The images show that the most of crystals are needle shape. However, it can be observed that SiO₂/Al₂O₃ = 16.3 shows some irregular shape of crystals and it has been in line with XRD pattern of unidentified phase in Figure 8. It also reveals that the product obtained from starting found at a higher SiO₂/Al₂O₃ has bigger needle-shaped crystals than that of low SiO₂/Al₂O₃.

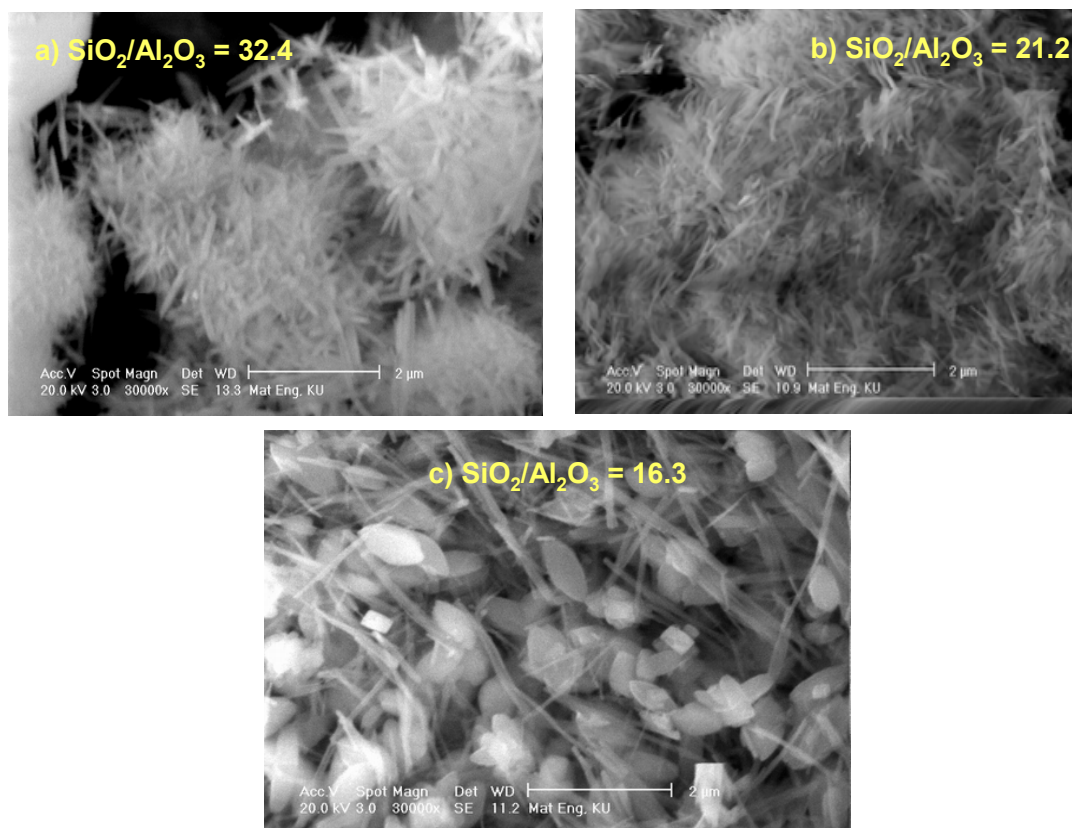


Figure 9 SEM images of zeolite SUZ-4 crystals prepared at 155 °C for 4 days with 300 rpm for different $\text{SiO}_2/\text{Al}_2\text{O}_3$ ratios (a) 32.4 (0.09 μm dia.x 0.63 μm long) (b) 21.2 (0.07 μm dia.x 0.64 μm long) (c) 16.3 (0.09 μm dia.x 1.20 μm long).

Subsequently, specific surface area, pore volume and pore diameter with different $\text{SiO}_2/\text{Al}_2\text{O}_3$ molar ratios were characterized by BET N_2 -adsorption/desorption isotherms as shown in Table 9. The resultant powder from gel mixture composition at $\text{SiO}_2/\text{Al}_2\text{O}_3$ of 21.2 having mainly SUZ-4 zeolite clearly possessed a high surface area at 440.4 m^2/g and large total pore volume of 1.036 cm^3/g . The result shows that specific surface area depends on type of zeolite.

Table 9 BET surface area and pore volume of synthesized zeolite with different SiO₂/Al₂O₃ ratios for 4 days crystallization.

SiO ₂ / Al ₂ O ₃	BET surface area (m ² /g)	External surface area ¹ (m ² /g)	Micropore surface area ¹ (m ² /g)	Micropore volume ¹ (cm ³ /g)	Total pore volume ² (cm ³ /g)	Pore diameter ³ (Å)
32.4	107.0	41.7	65.3	0.0269	0.1657	5.4
21.2	440.4	175.8	216.0	0.1089	1.0360	5.4
16.3	145.2	71.0	74.2	0.0332	0.1923	3.5

¹ t- plot micropore analysis method

² MP micropore analysis method at P/P₀ close to unity

³ SF micropore analysis method

The pore size distribution is presented in Figure 10 and it was indicated in narrow pore size distributions of SUZ-4 crystals. Saito-Foley (SF) method (Appendix C) is therefore used to calculate by micropore analysis in cylindrical pore geometry.

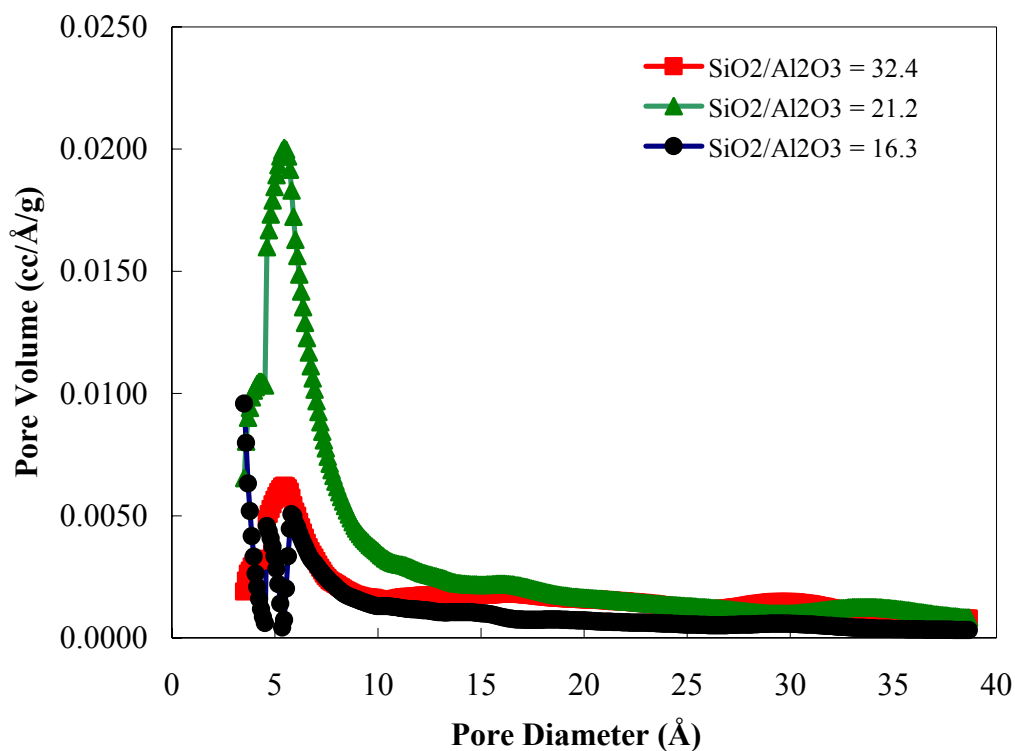


Figure 10 Pore size distribution (SF method) of SUZ-4 zeolite for 4 days crystallization with different $\text{SiO}_2/\text{Al}_2\text{O}_3$ ratios.

To confirm the characterization results, 2 days crystallization time was carried out in the same type of autoclave but higher reaction temperature at 169°C was controlled in the reactor. As shown in Table 10 and Figure 11, the results of SUZ-4 zeolite were mainly obtained from $\text{SiO}_2/\text{Al}_2\text{O}_3$ both of 32.7 and 21.2 ratios and they were found to have Si/Al (by weight) = 7-8.

Table 10 Effect of different $\text{SiO}_2/\text{Al}_2\text{O}_3$ at stirring around 300 rpm for 2 days crystallization.

No.	$\text{SiO}_2/\text{Al}_2\text{O}_3$	$\text{TEA}_2\text{O}/\text{Al}_2\text{O}_3$	$\text{H}_2\text{O}/\text{Al}_2\text{O}_3$	$\text{K}_2\text{O}/\text{Al}_2\text{O}_3$	Temp ($^\circ\text{C}$)	Product	Si/Al
14	32.69	3.11	783.98	7.30	169	SUZ-4+unidentified	~8.0
12	21.23	1.37	502.70	3.96	169	SUZ-4	~7.0
13	16.73	0.92	452.85	3.99	168	PHI+ unidentified	n/a
17	16.20	0.91	450.10	4.00	168	SUZ-4+PHI+ unidentified	n/a

Figure 11 shows XRD patterns with different $\text{SiO}_2/\text{Al}_2\text{O}_3$ for 2 days crystallization. It was found that using a $\text{SiO}_2/\text{Al}_2\text{O}_3$ ratio of 32.7 still gave some impurities of unidentified phase. Moreover, using low $\text{SiO}_2/\text{Al}_2\text{O}_3$ gave competing phillipsite (PHI) and unidentified phases as impurities of product on some experiments according to the results of Gujar and Price (2002). Gel mixture of $\text{SiO}_2/\text{Al}_2\text{O}_3 = 21.2$ under experiment conditions shows to be the good sample of mainly type of SUZ-4 zeolite with Si/Al (by weight) about 7.

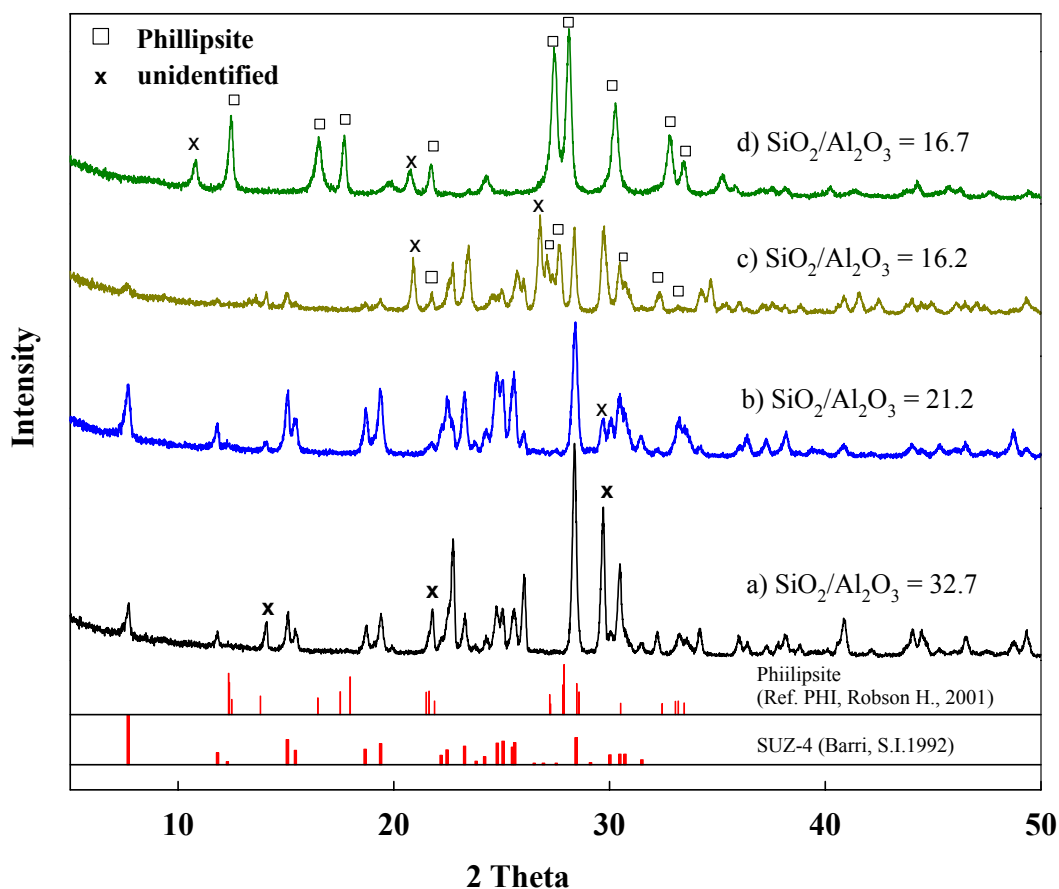


Figure 11 XRD patterns of zeolite SUZ-4 crystals prepared at 168 °C for 2 days with different SiO₂/Al₂O₃ (a) 32.7 (b) 21.2 (c) 16.2 (d) 16.7.

The SEM images in Figure 12 show that most crystals are still needle shape. However, it can be observed that SiO₂/Al₂O₃ = 16.2 shows some irregular shape and aggregated crystals and it has been in line with XRD pattern of phillipsite and unidentified phases in Figure 11. It also reveals that results of 2 days crystallization time were similar with 4 days, the product obtained at a higher SiO₂/Al₂O₃ has bigger needle-shaped crystals than that of low SiO₂/Al₂O₃.

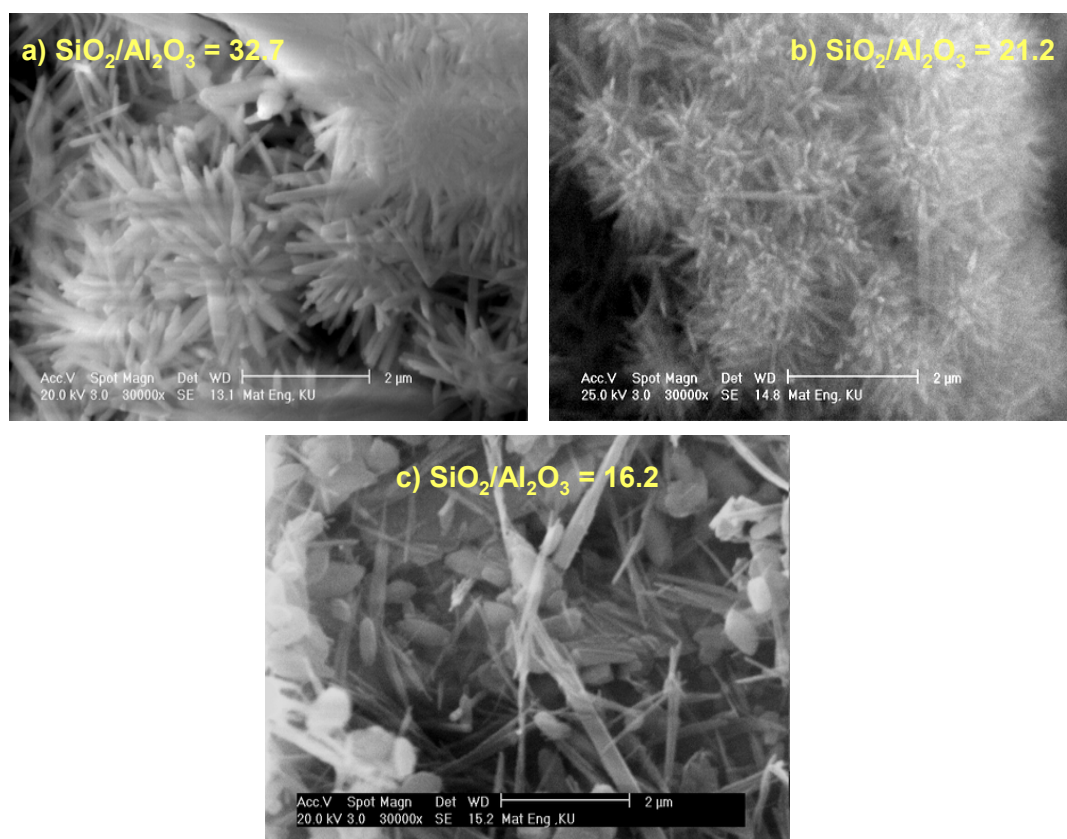


Figure 12 SEM images of zeolite SUZ-4 crystals prepared at 168 °C for 2 days with different SiO₂/Al₂O₃ (a) 33.3 (0.15 μm dia.x 1.09 μm long) (b) 21.2 (0.1 μm dia.x 0.41 μm long) (c) 16.2 (0.12 μm dia.x 1.23 μm long).

In addition, specific surface area and pore volume at different SiO₂/Al₂O₃ molar ratios for 2 days synthesis were characterized by BET N₂-adsorption/desorption isotherms shown in Table 11. The results clearly show that gel mixture composition with SiO₂/Al₂O₃ = 21.2 for 2 days can yield high BET surface area 347.6 m²/g and total pore volume was 0.3692 cm³/g. However, it can be seen that physical properties of micropore surface area and micropore volume under the condition of SiO₂/Al₂O₃ = 21.2 prepared at 155 °C for 4 days (Table 9) show better results than SiO₂/Al₂O₃ = 21.2 prepared at 168 °C for 2 days crystallization time (Table 11).

Table 11 BET surface area and pore volume of synthesized with different $\text{SiO}_2/\text{Al}_2\text{O}_3$ ratios zeolite for 2 days crystallization.

$\text{SiO}_2/\text{Al}_2\text{O}_3$	BET surface area (m^2/g)	External surface area ¹ (m^2/g)	Micropore surface area ¹ (m^2/g)	Micropore volume ¹ (cm^3/g)	Total pore volume ² (cm^3/g)	Pore diameter ³ (\AA)
33.3	76.0	70.7	5.3	0.0071	0.1441	5.4
21.2	347.6	197.2	84.5	0.0558	0.3692	5.4
16.2	18.4	18.4	0	0	0.1046	3.5

¹ t- plot micropore analysis method

² MP micropore analysis method at P/P_0 close to unity

³ SF micropore analysis method

The pore size distributions shown in Figure 13 indicate the narrow distributions same as the previous results.

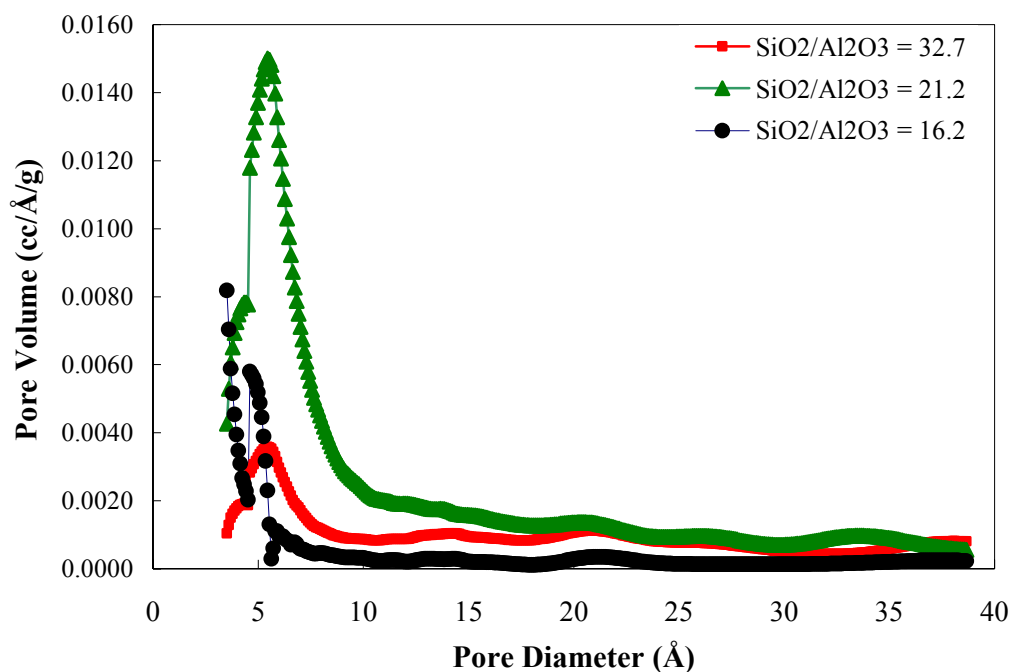


Figure 13 Pore size distribution (SF method) of SUZ-4 zeolite for 2 days crystallization with different $\text{SiO}_2/\text{Al}_2\text{O}_3$ ratios.

Figure 14 shows XRD patterns comparison between 4 days and 2 days crystallization time of SUZ-4 zeolite prepared at $\text{SiO}_2/\text{Al}_2\text{O}_3 = 21.2$, using 2 days synthesis time gave unidentified phase as impurity of product.

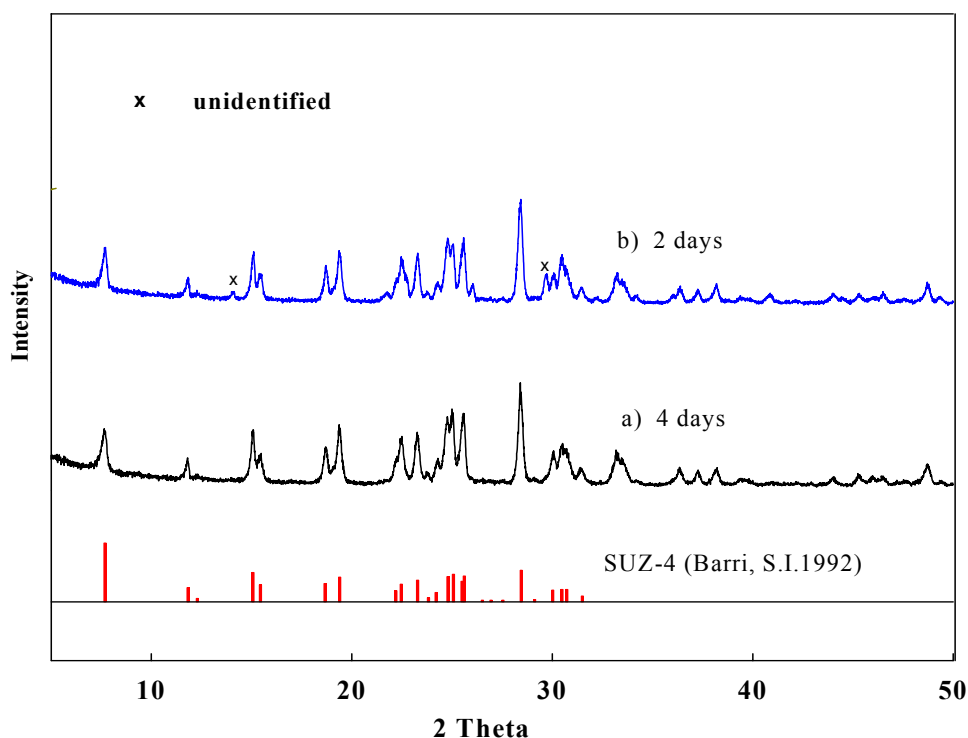


Figure 14 XRD patterns comparison between 4 days and 2 days crystallization time of SUZ-4 zeolite prepared at $\text{SiO}_2/\text{Al}_2\text{O}_3 = 21.2$.

In conclusion, the results from characterization of SUZ-4 zeolite reveal that gel mixture composition, stirring speed, crystallization time and temperature affect on crystal physical properties. It can be seen that the vigorous stirring at 300 rpm with 155°C for 4 days crystallization time on $\text{SiO}_2/\text{Al}_2\text{O}_3 = 21.2$ gave good characteristic. Therefore, it is suitable to reproduce SUZ-4 zeolite under these conditions using home-made design autoclaves (390 ml Teflon-lined home-made design stainless steel autoclave with circulating air drying oven (Forced convection BINDER GmbH Model FP240, Germany)). It can produce zeolite powder and zeolite-coated membrane at the same time. Crystals (zeolite powder) can be recovered from the bottom of the reactor.

1.3 Reproducible SUZ-4 Zeolite Powder and Zeolite Membrane Synthesis

The gels were crystallized at 155 °C and rotation at 30 rpm with homogeneity instead of stirring at 300 rpm. The stirring or rotation rate depends on type of autoclaves following the experiment previously described (Asensi *et al.*, 1999). The relative amount of KOH, TEAOH, LUDOX AS-40 colloidal silica and aluminum metal were maintained. The gel composition can be expressed as $4.0\text{K}_2\text{O}:\text{Al}_2\text{O}_3:21.2\text{SiO}_2:1.3\text{TEA}_2\text{O}:1,198-2,554\text{H}_2\text{O}$.

1.3.1 The Effect of $\text{H}_2\text{O}/\text{Al}_2\text{O}_3$ on SUZ-4 zeolite powder

First, the obtained SUZ-4 powder from synthesis was discussed. As shown in Table 12, SUZ-4 zeolite powder was obtained under $\text{H}_2\text{O}/\text{Al}_2\text{O}_3 = 1,198-1,351$ during crystallization time of 3.9 days to 4.9 days and Si/Al (by weight) is in the range of 6.8-7.7, but the result shows that SUZ-4 zeolite cannot be produced at high $\text{H}_2\text{O}/\text{Al}_2\text{O}_3$ ratio of 2,554.

Table 12 Conditions and results for reproducible SUZ-4 synthesis with different H₂O/Al₂O₃ ratios

No.	SiO ₂ / Al ₂ O ₃	TEA ₂ O/ Al ₂ O ₃	H ₂ O/ Al ₂ O ₃	K ₂ O/ Al ₂ O ₃	Time (day)	Product	Si/Al
M1	21.25	1.30	1201.81	4.02	4	SUZ-4	n/a
M1S	21.24	1.30	1201.87	4.01	4	SUZ-4	7.5
M2	21.22	1.30	1201.58	3.98	4	SUZ-4	6.8
M2S	21.23	1.30	1201.66	4.01	4	SUZ-4	6.9
M3	21.32	1.30	2554.21	4.01	4	amorphous	n/a
M3S	21.29	1.31	2554.18	4.01	4	amorphous	n/a
M4	21.17	1.30	1197.77	4.00	3.9	SUZ-4	7.7
M4S	21.21	1.30	1199.73	3.97	3.9	SUZ-4	7.5
M5	21.17	1.30	1351.39	4.00	4.9	SUZ-4	7.3
M5S	21.18	1.30	1351.45	3.96	4.9	SUZ-4	7.4

Figure 15 shows XRD patterns from reproducible synthesis under controlled conditions with different H₂O/Al₂O₃. It can be seen that gel composition with excess H₂O/Al₂O₃ ratio at 2,554 cannot produce SUZ-4 zeolite, but the amorphous phase was obtained as shown in Figure 15c. This indicates that H₂O/Al₂O₃ ratio is also one of key factors for synthesis.

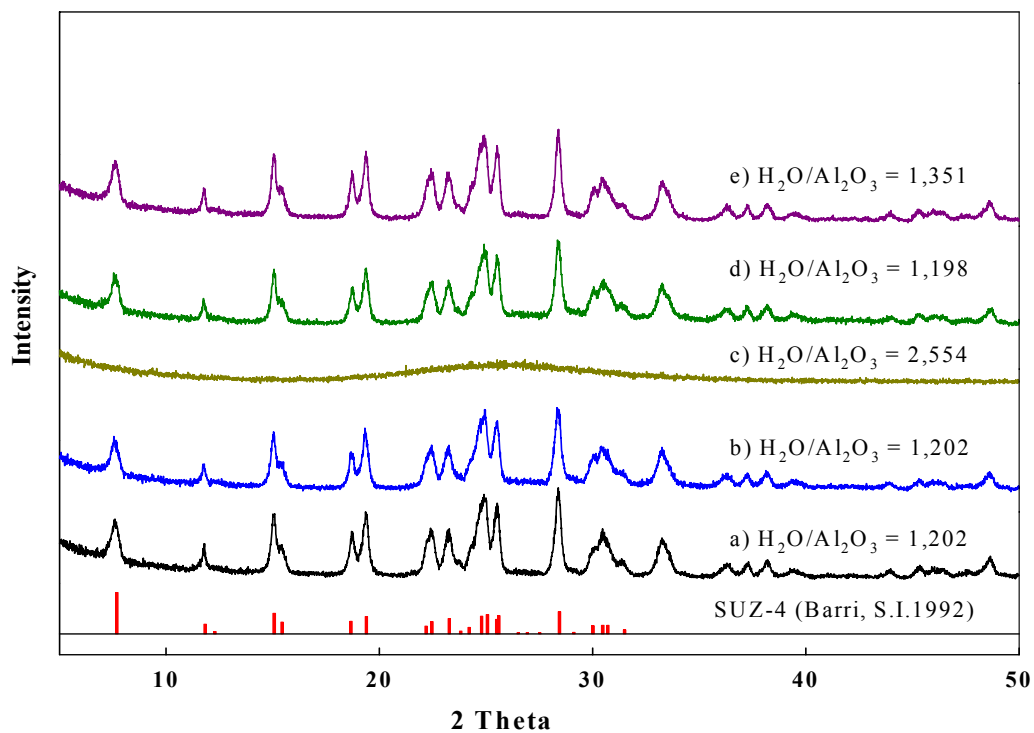


Figure 15 XRD patterns of reproducible SUZ-4 zeolite powder synthesis prepared with different $\text{H}_2\text{O}/\text{Al}_2\text{O}_3$ ratios.

SEM images of SUZ-4 zeolite powder show needle-shape crystal in both without and with seeding for SUZ-4 zeolite membrane synthesis in Figure 16 and Figure 17, respectively. For zeolite powder, the results from SEM images with seed and without seed were not much different crystals.

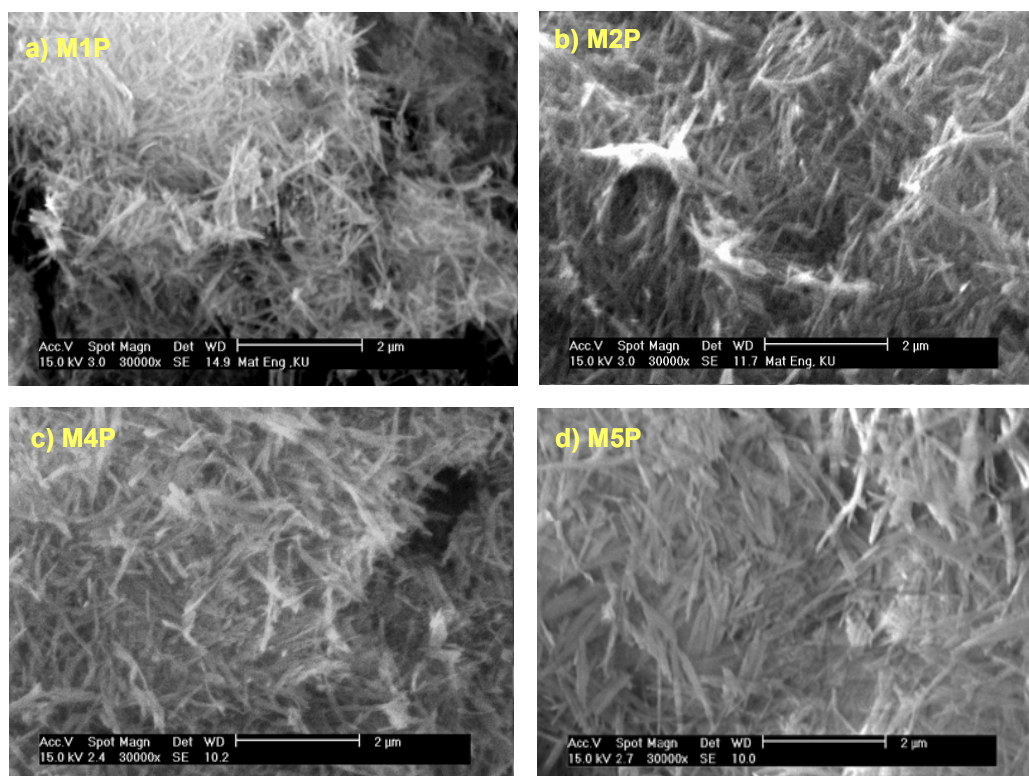


Figure 16 SEM images of zeolite SUZ-4 crystals prepared without seeding
(a) M1P (0.06 μm dia.x 0.62 μm long) (b) M2P (0.07 μm dia.x 0.63 μm long) (c) M4P (0.1 μm dia.x 0.65 μm long) (d) M5P (0.1 μm dia.x 0.97 μm long).

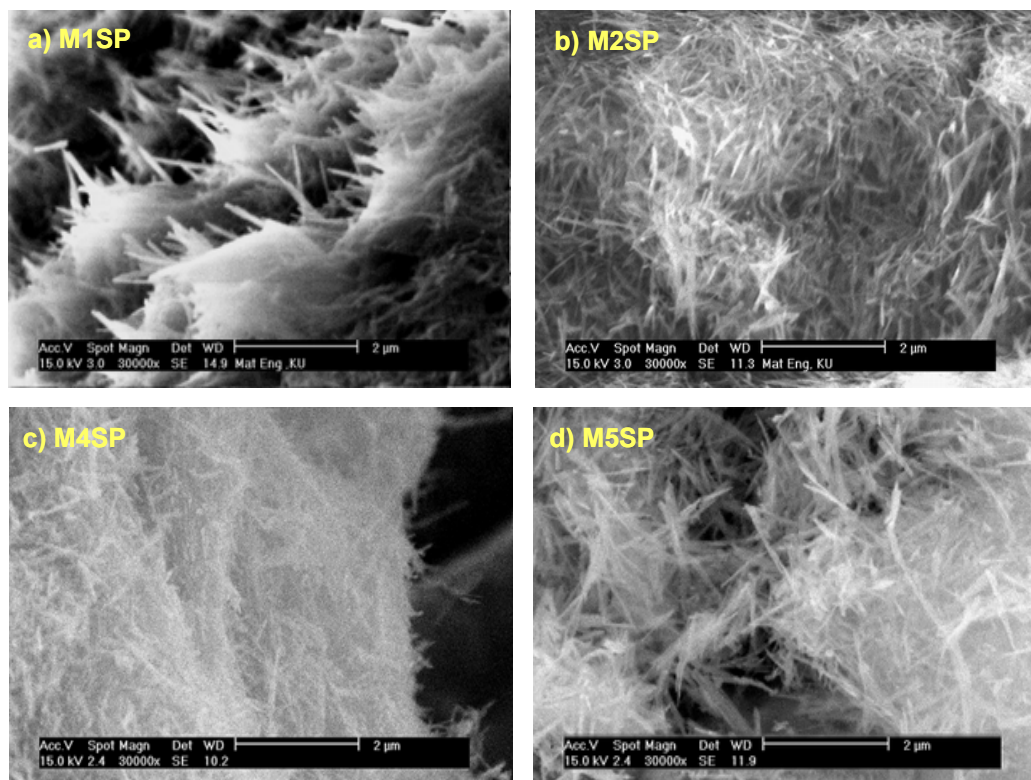


Figure 17 SEM images of zeolite SUZ-4 crystals prepared with seeding

- (a) M1SP (0.09 μm dia. x 0.83 long) (b) M2SP (0.07 μm dia. x 0.51 long)
 (c) M4SP (0.08 μm dia. x 0.63 long) (d) M5SP (0.08 μm dia. x 0.7 long).

Subsequently, specific surface area and pore volume for reproducible SUZ-4 synthesis at $\text{SiO}_2/\text{Al}_2\text{O}_3 = 21.2$ condition were carried out by BET N_2 -adsorption/desorption isotherms as shown in Table 13. The results in Table 13 clearly confirmed that this gel mixture composition at $\text{SiO}_2/\text{Al}_2\text{O}_3$ of 21.2 from owned designed reactors still obtained the similar results in synthesis from Parr Model 4561 having high BET surface area ranging 370-422 m^2/g and total pore volume was in the range of 0.2642-2.611 cm^3/g .

Table 13 BET surface area and pore volume of reproducible zeolite at $\text{SiO}_2/\text{Al}_2\text{O}_3 = 21.2$ with different $\text{H}_2\text{O}/\text{Al}_2\text{O}_3$ ratios.

No.	BET surface area (m^2/g)	External surface area ¹ (m^2/g)	Micropore surface area ¹ (m^2/g)	Micropore volume ¹ (cm^3/g)	Total pore volume ² (cm^3/g)	Pore diameter ³ (\AA)
M1	369.5	295.5	74.1	0.0648	0.2642	5.6
M1S	422.2	336.5	85.7	0.0711	1.109	5.4
M2	390.6	312.3	78.3	0.0681	1.910	5.8
M2S	407.5	582.2	68.7	0.0644	2.368	5.4
M4	378.6	304.5	74.1	0.0661	1.766	3.5
M4S	430.2	342.0	88.2	0.0733	0.4469	5.8
M5	391.5	296.5	95.0	0.0742	1.684	5.7
M5S	396.4	311.6	84.8	0.0696	2.611	3.5

¹t- plot micropore analysis method

²MP micropore analysis method at P/P_0 close to unity, except No.M4S at $P/P_0=0.9492$

³SF micropore analysis method

The pore size distributions shown in Figure 18 indicate the narrow distributions same as the previous results.

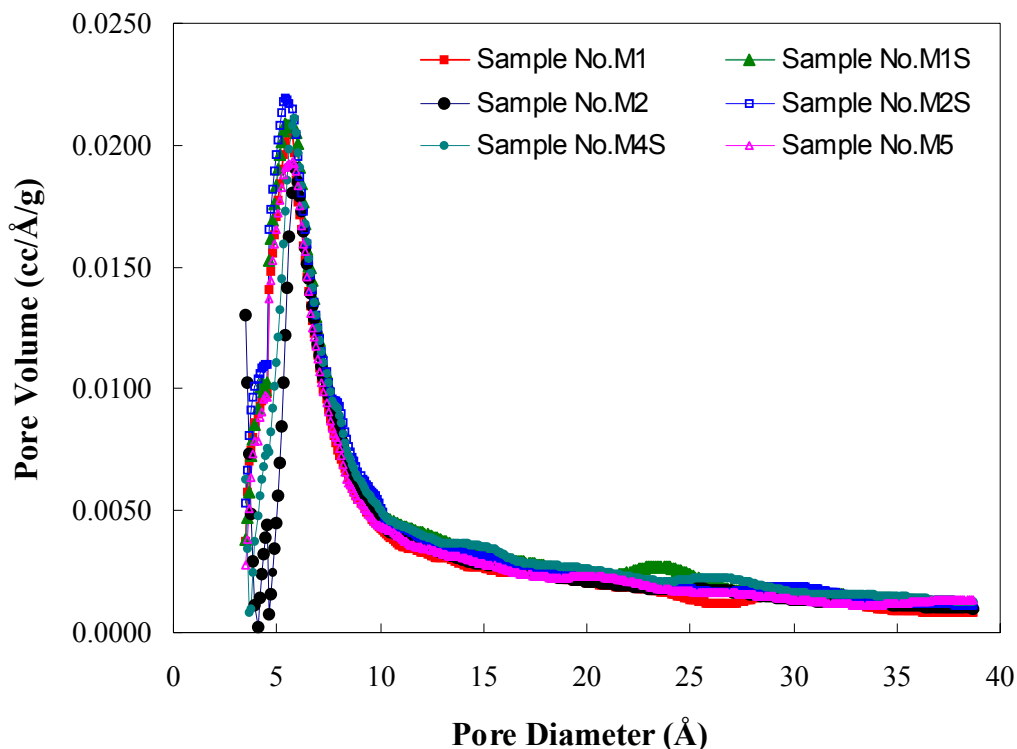


Figure 18 Pore size distribution (SF method) of reproducible SUZ-4 zeolite powder of $\text{SiO}_2/\text{Al}_2\text{O}_3 = 21.2$ with different conditions.

1.3.2 The Effect of SUZ-4 seeding on SUZ-4 zeolite membrane thickness and crystal size

Mullite tube was used as a supporter for synthesis of SUZ-4 zeolite layer. Pore size and porosity were monitored by mercury intrusion porosimetry (PoreMaster 33, Quantachrome). The result shows that pore diameter of mullite was about $89.80 \mu\text{m}$ having porosity of 21%.

Crystallization with or without seeding can affect on SUZ-4 zeolite membrane (zeolite layer on the outer supporter) in the same reactors. The results from SEM images observation show that the thickness of zeolite membrane without seeding (Figure 19a and 19b) was about $19 \mu\text{m}$ while the thickness of synthesis with seeding (Figure 19c and 19d) was about $84 \mu\text{m}$.

However, some leaks on designed reactor for first experiment without seeding No.M1 (Table 1) was found after crystallization for 4 days. Therefore, it may cause the error of the thickness of SUZ-4 zeolite layer in over number as should it be when comparing to the one with seeding.

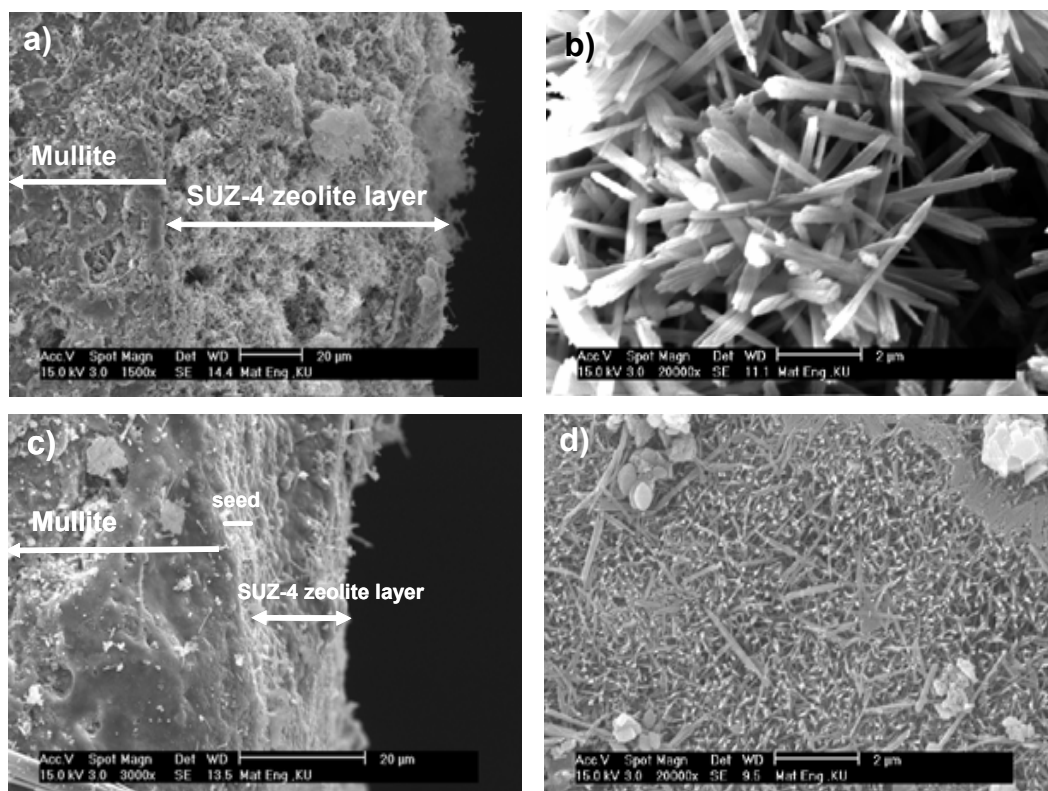


Figure 19 SEM images of SUZ-4 zeolite membrane prepared for 4 days with $\text{SiO}_2/\text{Al}_2\text{O}_3 = 21.2$ cross-section and top view (a) M1 cross-section (84 μm thickness) (b) M1 top view of SUZ-4 crystals (0.27 μm dia. x 4 μm long) and (c) M1S cross-section (19 μm thickness) (d) M1S top view of SUZ-4 crystals (0.07 μm dia. x 0.52 μm long).

After the leakage reactor was fixed, the condition was then repeated the same conditions for 4 days crystallization (No. M2). The results show that SUZ-4 zeolite with seeding (Figure 20c and 20d) can give more thickness than without seeding (Figure 20a and 20b). As shown in Figure 20c, SEM cross section image

show thickness of SUZ-4 zeolite layer with seeding was about 14 μm and the thickness of synthesis without seeding (Figure 20a) was about 4 μm . It can be implied that seeds or existing crystals can be the secondary nucleation growth and can assist the crystallization. Top view images shown SUZ-4 zeolite crystals have been stacked together.

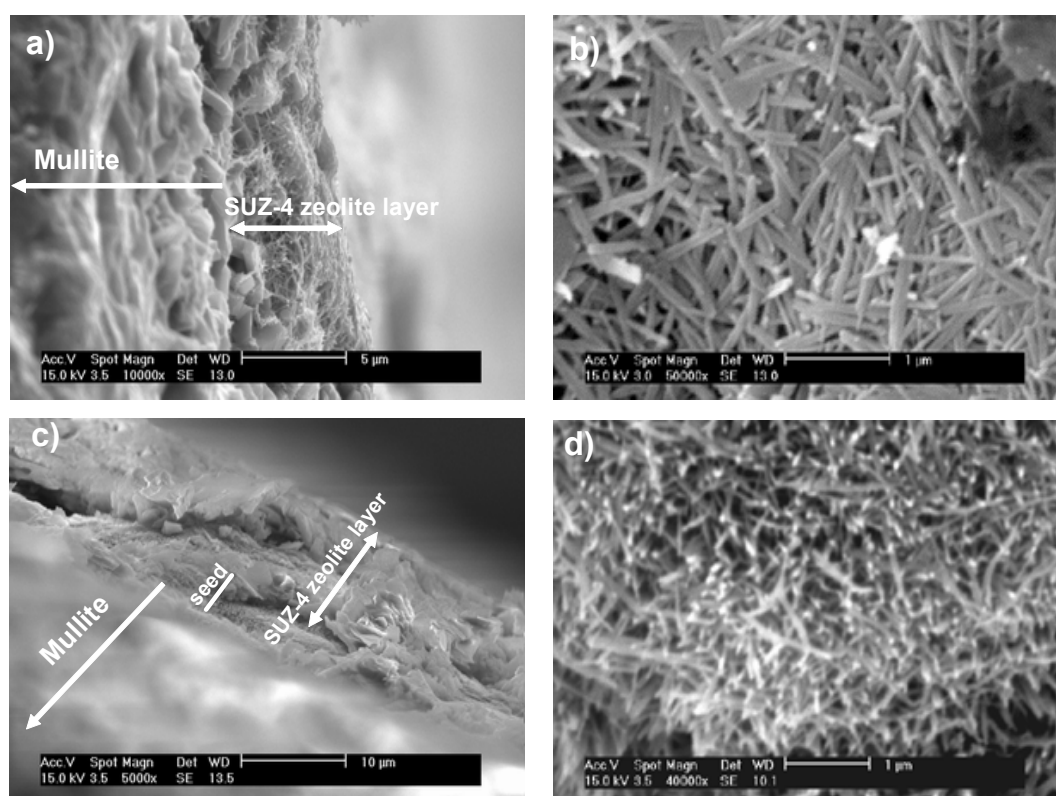


Figure 20 SEM images of SUZ-4 zeolite membrane re-prepared for 4 days with $\text{SiO}_2/\text{Al}_2\text{O}_3 = 21.2$ cross-section and top view (a) M2 cross-section (4 μm thickness) (b) M2 top view of SUZ-4 crystals (0.08 μm dia. x 0.6 μm long) (c) M2S cross-section (14 μm thickness) (d) M2S top view of SUZ-4 crystals (0.07 μm dia. x 0.47 μm long).

As shown in Figure 21, synthesis of SUZ-4 zeolite membrane with seeding has still more thickness than without seeding. In addition, the crystal sizes of SUZ-4 in needle shape were not much different in each experiment. However, top

view images show that SUZ-4 crystals were not in perfect order arrangement and they have not been stacked together under those conditions.

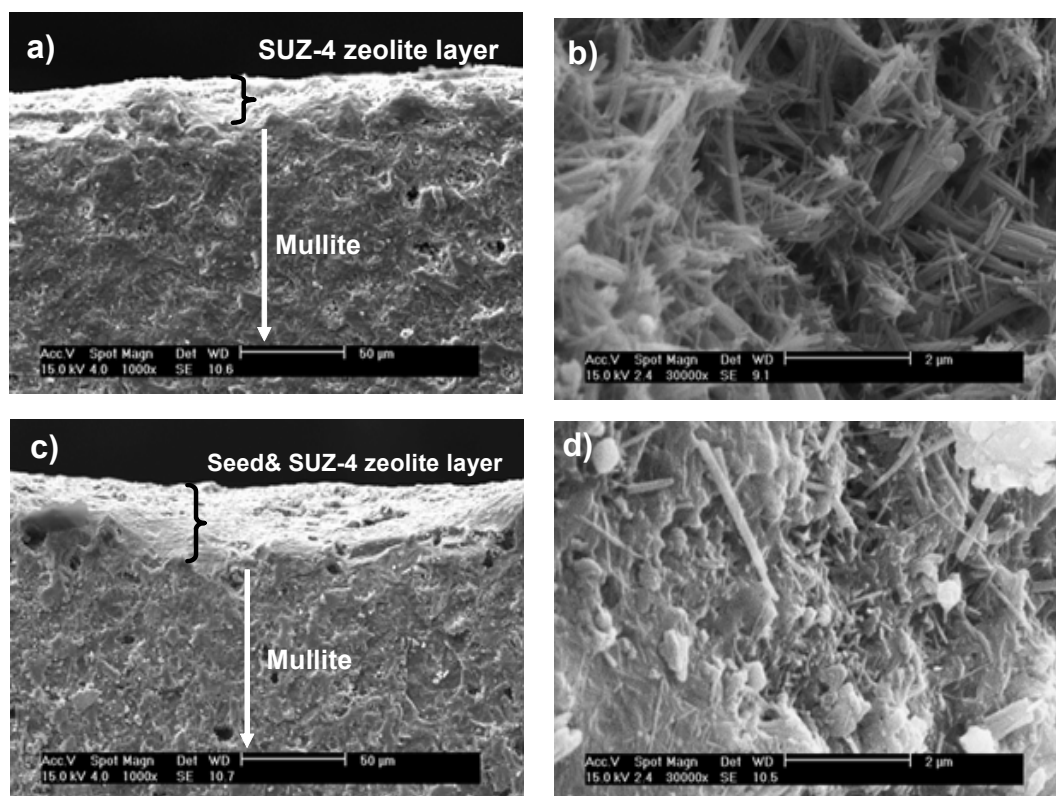


Figure 21 SEM images of SUZ-4 zeolite membrane prepared for 3.9 days with $\text{SiO}_2/\text{Al}_2\text{O}_3 = 21.2$ cross-section and top view (a) M4 cross-section (17.5 μm thickness) (b) M4 top view of SUZ-4 crystals (0.07 μm dia. x 0.73 μm long) (c) M4S cross-section (24.8 μm thickness) (d) M4S top view of SUZ-4 crystals (0.07 μm dia. x 0.71 μm long).

The results from increasing crystallization time of SUZ-4 zeolite membrane to 4.9 days were shown in Figure 22. It was observed that longer synthesis time under controlled the same conditions can give more thickness and larger crystal size.

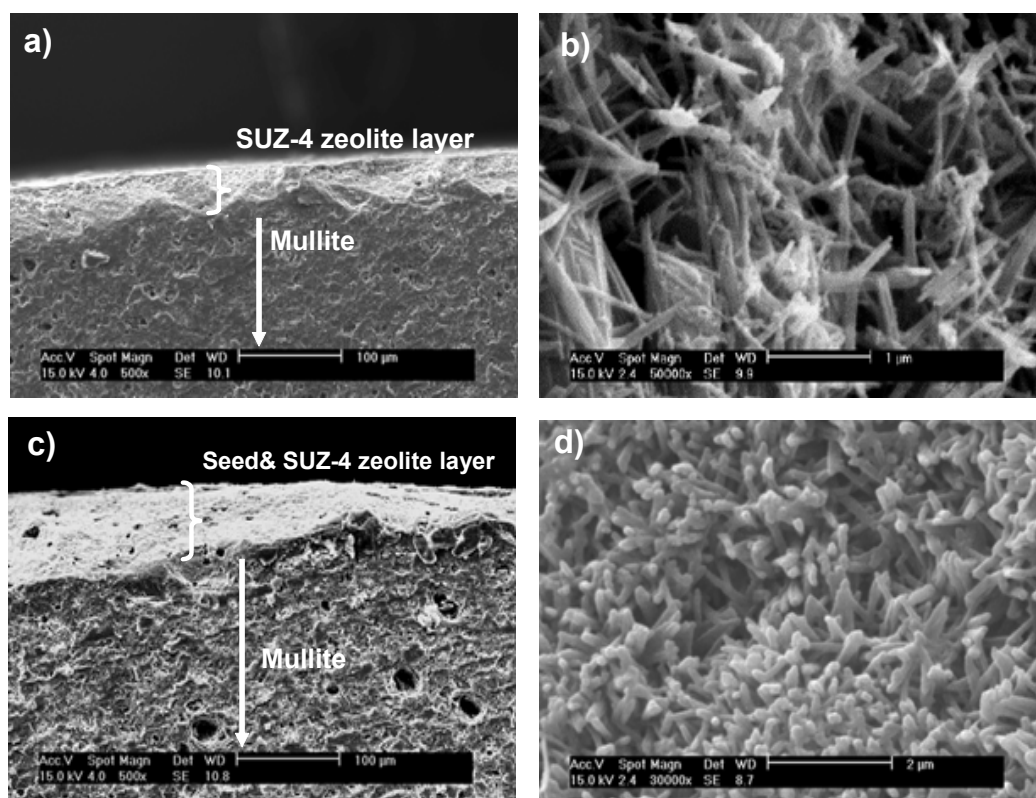


Figure 22 SEM images of SUZ-4 zeolite membrane prepared for 4.9 days with $\text{SiO}_2/\text{Al}_2\text{O}_3 = 21.2$ cross-section and top view (a) M5 cross-section (41 μm thickness) (b) M5 top view of SUZ-4 crystals (0.1 μm dia.x 0.88 μm long) (c) M5S cross-section (54 μm thickness) (d) M5S top view of SUZ-4 crystals (0.097 μm dia.x 0.76 μm long).

In conclusion, top view can confirm SUZ-4 zeolite coating on each membrane. The results were observed that SUZ-4 membrane with seeding can have smaller size of needle zeolite crystals.

These experiments were preliminary successful result for SUZ-4 zeolite membrane. Zeolite membrane synthesis is harder than powder synthesis and special shape of SUZ-4 zeolite is needle-shaped crystal. Therefore, the systematic experiments of synthesis in crystal orientation, plane deposition and surface charge between supporter and zeolite should be concerned and developed to further study.

1.4 Bonding analysis from FTIR of SUZ-4 Zeolite

Figure 23 shows FTIR spectrum in the region of 4000-400 cm^{-1} for the powder sample under 155 °C hydrothermal for 4 days with $\text{SiO}_2/\text{Al}_2\text{O}_3 = 21.2$ (No. M2S). As it is well known that the thermal stability of zeolite is related to the defect sites, i.e., the number of silanol groups, within zeolite crystal, thus the FT-IR spectra of uncalcined and calcined SUZ-4 zeolites synthesized were observed. The peaks at 3741 and 3603 cm^{-1} are assigned to isolated silanol groups and acidic bridged OH of $\text{Si}(\text{OH})\text{Al}$, respectively (Zholobenko *et al.*, 1998; Lukyanov *et al.*, 1999). Frequencies of $\text{Si}(\text{OH})\text{Al}$ group vibration in zeolites depend generally on local structure and composition. There is IR spectroscopic evidence for the presence of different peaks between before and after calcinations. Absorbed water bonding at 3000 cm^{-1} still shows for uncalcined while no peak for calcined SUZ-4. Moreover, the vibration bonding results clearly show that some position disappeared for calcined sample when compared to uncalcined one that still have TEAOH in the sample.

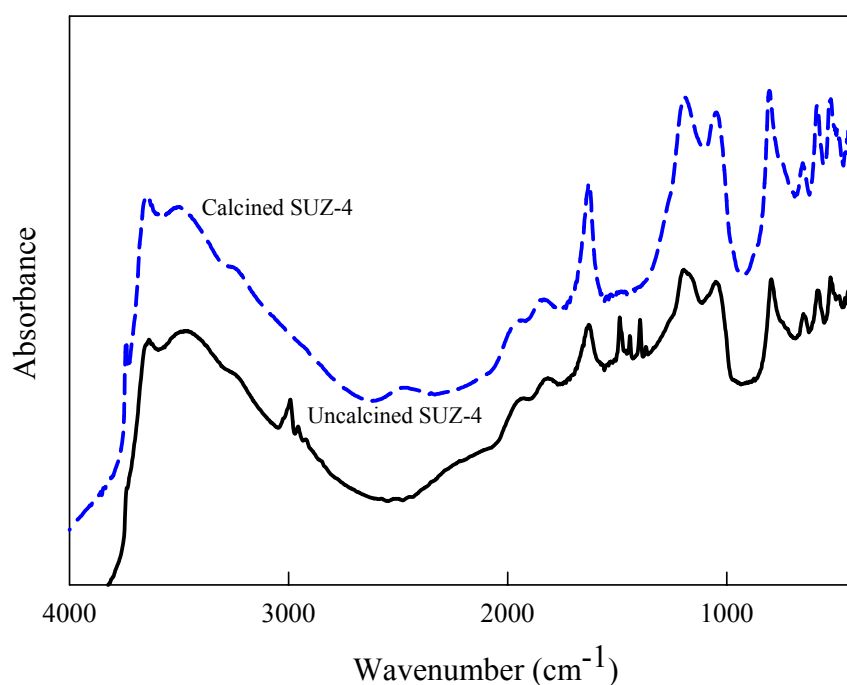


Figure 23 FTIR spectra of as-synthesized SUZ-4 zeolite obtained from M2S powder. for uncalcined and calcined SUZ-4 zeolites.

1.5 Zeta Potential Studies of SUZ-4 Zeolite

Figure 24 shows zeta potential values as a function of pH for mullite supporter and as-synthesized SUZ-4 zeolite. It is observed that there is no iso-electric point (IEP) of SUZ-4 zeolite powder at pH 2-12 in distilled water and zeolite remains negative charged in this range. This result from zeta potential shows colloidal stability of the suspensions of SUZ-4. Mullite supporter was shown the result in an IEP at pH about 5.88 and mostly is also in the negative surface charge. Since no additional background electrolyte was used to enhance the ionic strength, the measured zeta potential for zeolite layer closely follows the surface charge of SUZ-4 zeolite crystal in suspension.

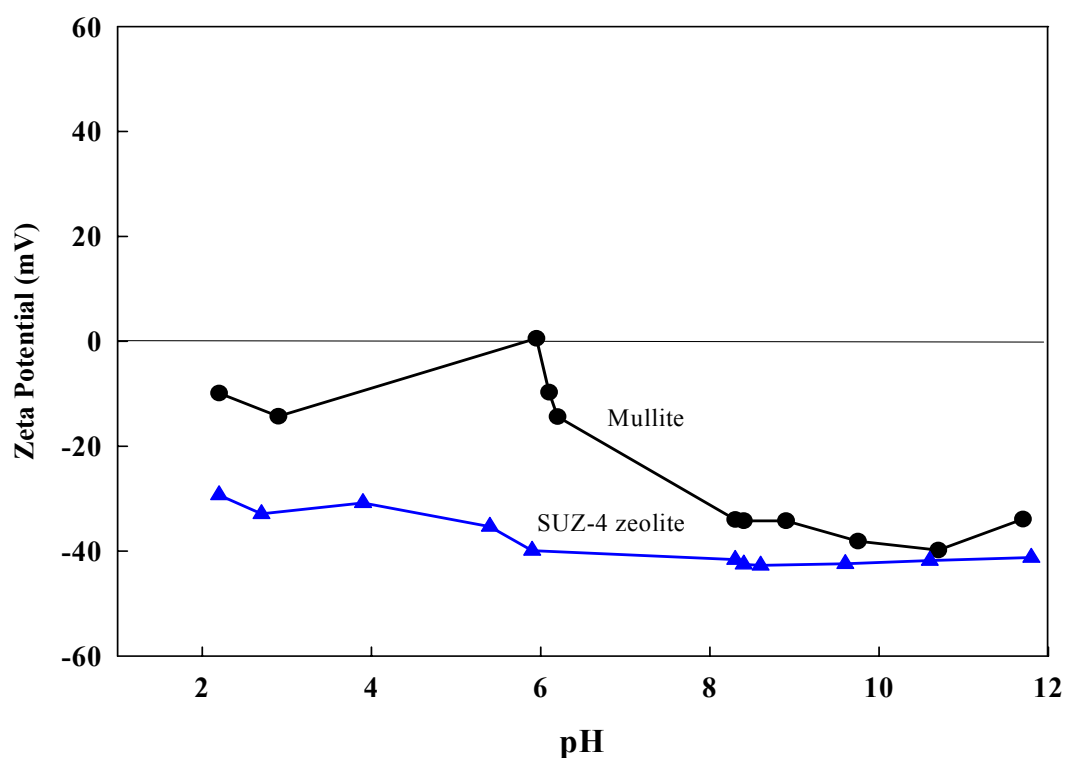


Figure 24 Zeta potential of mullite supporter and as-synthesized SUZ-4 zeolite powder as a function of pH.

2. Part II: SiO₂-TiO₂ and SiO₂-Al₂O₃ Nanostructured Composites Synthesis

The results on SiO₂-TiO₂ nanocomposite are presented first and followed by the SiO₂-Al₂O₃ system. The effect of precursor molar ratio on crystal phase and the effect of quench ring position on specific surface area and morphology were discussed. The chemical bonding and surface charge of nanocomposite materials were also pointed out.

2.1 SiO₂-TiO₂ System

2.1.1 Effect of Si:Ti molar ratio

The addition of SiO₂ into TiO₂ can control phase transition. To control Si:Ti precursor molar ratio, TEOS precursor concentration was changed by varying the evaporating temperature of TEOS while the TTIP precursor concentration was kept the same. As shown in Table 14, the effect of Si:Ti precursor concentration mole ratio was examined in the range from 0.27 to 17.5 for nanocomposite material compared to pure SiO₂ and pure TiO₂. Assuming all particles having spherical shape and monodispersion, the BET-equivalent particle diameter (d_{BET}) can be calculated based on the specific surface area (SSA) and the particle density (ρ) by $d_{\text{BET}} = 6/(\rho * \text{SSA})$ (Lindackers *et al.*, 1998; Wegner and Pratsinis, 2003; Akurati *et al.*, 2006).

Table 14 Specific surface area and particle size variation for different Si and Ti precursor feed rates.

No.	Precursor molar ratio	Phase composition ¹	SSA ² (m ² /g)	d _p ² (nm)
1	Pure SiO ₂	Amorphous SiO ₂	163.16	14.1
2	Si:Ti=17.5	Amorphous SiO ₂	42.40	54.4
3	Si:Ti=4	Amorphous SiO ₂ +100% anatase	35.53	57.6
4	Si:Ti =1.39	Amorphous SiO ₂ +74% anatase	39.89	46.3
5	Si:Ti = 0.27	Amorphous SiO ₂ +76% anatase	35.85	43.7
6	Pure TiO ₂	61% Rutile + 39% anatase	27.54	54.4

¹ From XRD

² From BET, multiple point

Figure 25 clearly shows that the intensities of the rutile peak decrease with increasing SiO₂. The weight fractions of anatase phase shown in Table 14 were calculated from relative intensities of major peaks corresponding to anatase and rutile as described by Spurr and Myers (1975). Based on the calculation, it indicates that 39 % by weight of pure TiO₂ is anatase. When Si:Ti precursor molar ratio was 4, 100% anatase was obtained. As a result, it was found that addition of SiO₂ to TiO₂ inhibited phase transformation of anatase to rutile. This may be due to the difference of ionic radius between Ti⁴⁺ (0.61 Å) and Si⁴⁺ (0.40 Å). Si⁴⁺ is small enough to enter TiO₂ lattice interstitially preventing the phase transformation (Vemury and Pratsinis, 1995). In addition, when the ratio of Si:Ti was changed from 4 to 17.5, XRD pattern shows only amorphous SiO₂ without any TiO₂ peak. It reveals that the SiO₂ content absolutely suppressed crystalline TiO₂.

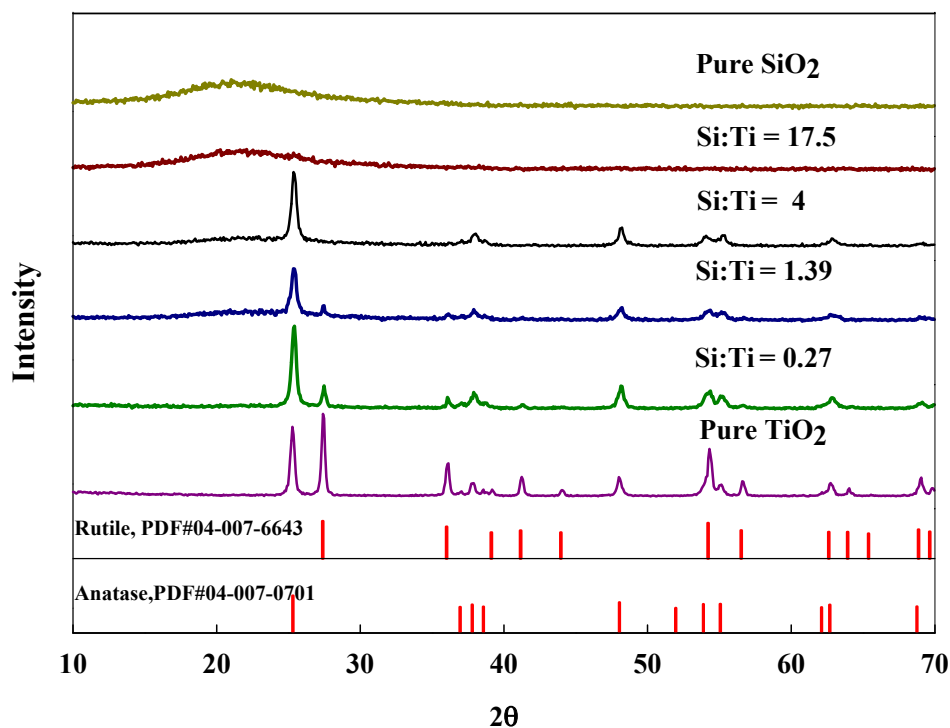


Figure 25 XRD patterns of composite SiO₂-TiO₂ powder prepared at 4 inch quench ring position with different precursor molar ratios.

Regarding the specific surface area of the obtained nanocomposites, it was found that the surface area slightly increased with increasing SiO₂ content and their sizes were in the range of 43.7 to 57.6 nm (Table 14). As pure phase, synthesized SiO₂ had much larger surface area and smaller particle size than that of TiO₂.

2.1.2 Effect of quench ring position

The quenching process of the flame aerosol has been used to precisely control particle size and morphology (Wegner and Pratsinis, 2003). In this work, as shown in Figure 26, while Si:Ti was set at 4 and quench ring position was increased from 1 to 8 inch, specific surface area (SSA) decreased and larger particle size (d_{BET}) was observed. The effect of ring position on specific surface area with 1

lpm of CH₄ yielded the similar results as that of 1.8 lpm of CH₄. This is because longer residence time in high temperature zone allowed the completion of sintering or coalescence of the nanoparticles. According to the formation of nanoparticles at high temperature (Figure 4), the TTIP vapor decomposed to TiO₂ monomer molecules which then formed stable TiO₂ nanoparticles. After the agglomeration of TiO₂ particles, silica vapors nucleated and coated on TiO₂ to form a core-shell structure or solid mixture of SiO₂-TiO₂ nanocomposite particle.

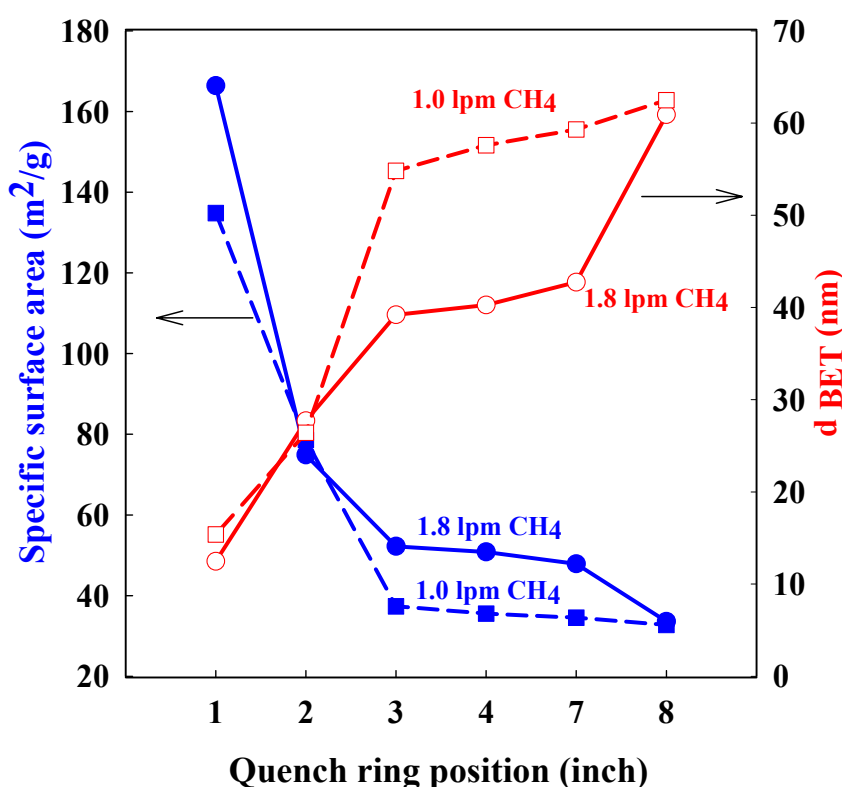


Figure 26 Specific surface area and particle size as a function of quench ring position (at precursor molar ratio Si:Ti= 4) at CH₄ flowrate of 1 and 1.8 lpm.

In this study, TiO₂ coated with SiO₂ was clearly obtained at low quench ring position. Because TTIP has lower thermal decomposition temperature than TEOS, TiO₂ particles were formed first. Then, SiO₂ no longer had enough time sintering and coalescing; subsequently, it condensed on TiO₂ crystal and formed the core-shell structure of SiO₂-TiO₂ (Figure 27a and 27c).

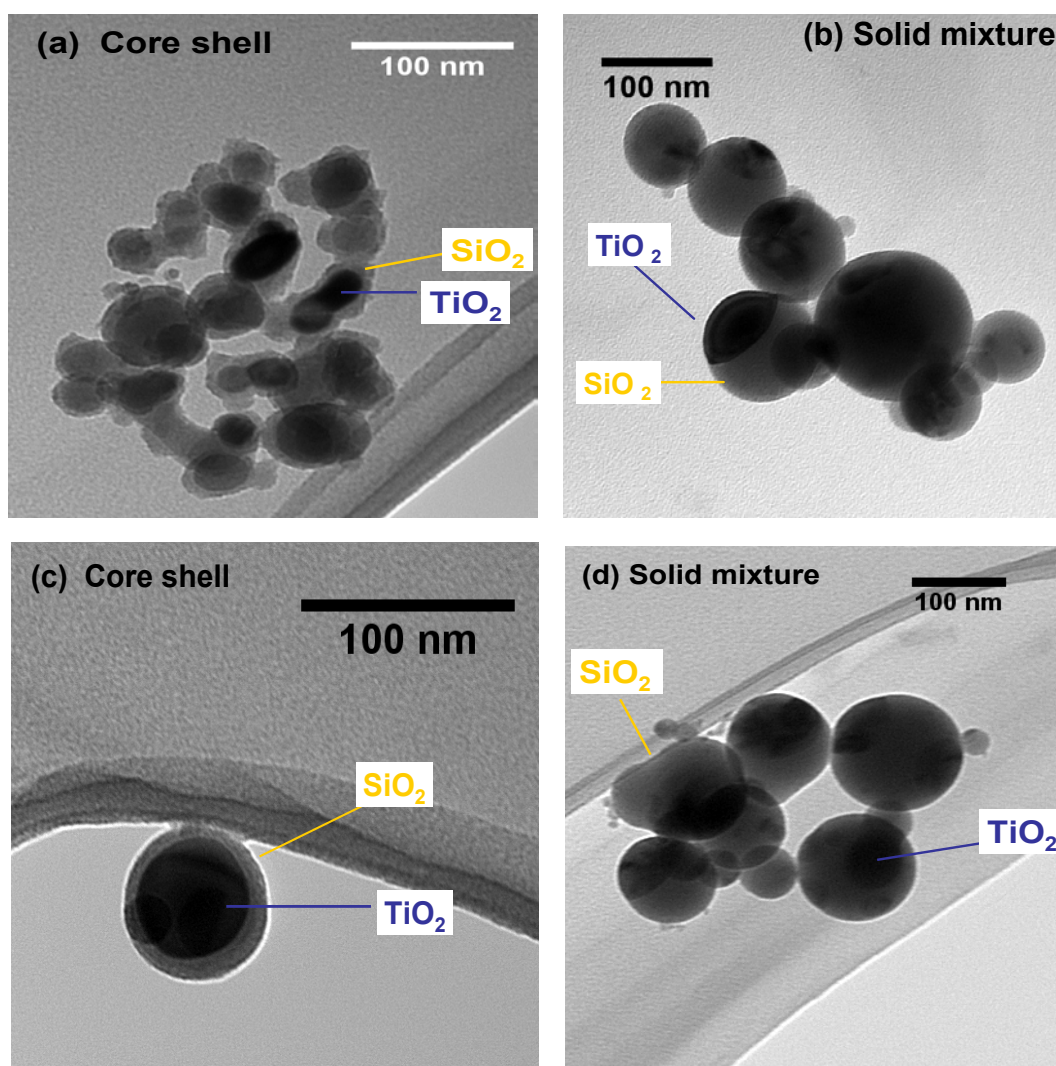


Figure 27 TEM images of SiO₂-TiO₂ composite molar ratio of Si:Ti = 4 prepared with different quench ring positions (a) 2 inch at 1.8 lpm CH₄ flowrate (b) 7 inch at 1.8 lpm CH₄ flowrate (c) 2 inch at 1.0 lpm CH₄ flowrate (d) 7 inch at 1.0 lpm CH₄ flowrate.

At high quench ring position, TEM images (Figure 27c and 27d) show that SiO₂ get into TiO₂ structure to form solid mixture particles as also confirmed by XRD patterns that show only anatase (Figure 28b). On the other hand, XRD patterns still show both rutile and anatase peaks in pure TiO₂ at high quench

ring position (Figure 28a). Thus, it can be concluded that the addition of SiO_2 in TiO_2 to form SiO_2 - TiO_2 nanocomposite can inhibit rutile phase.

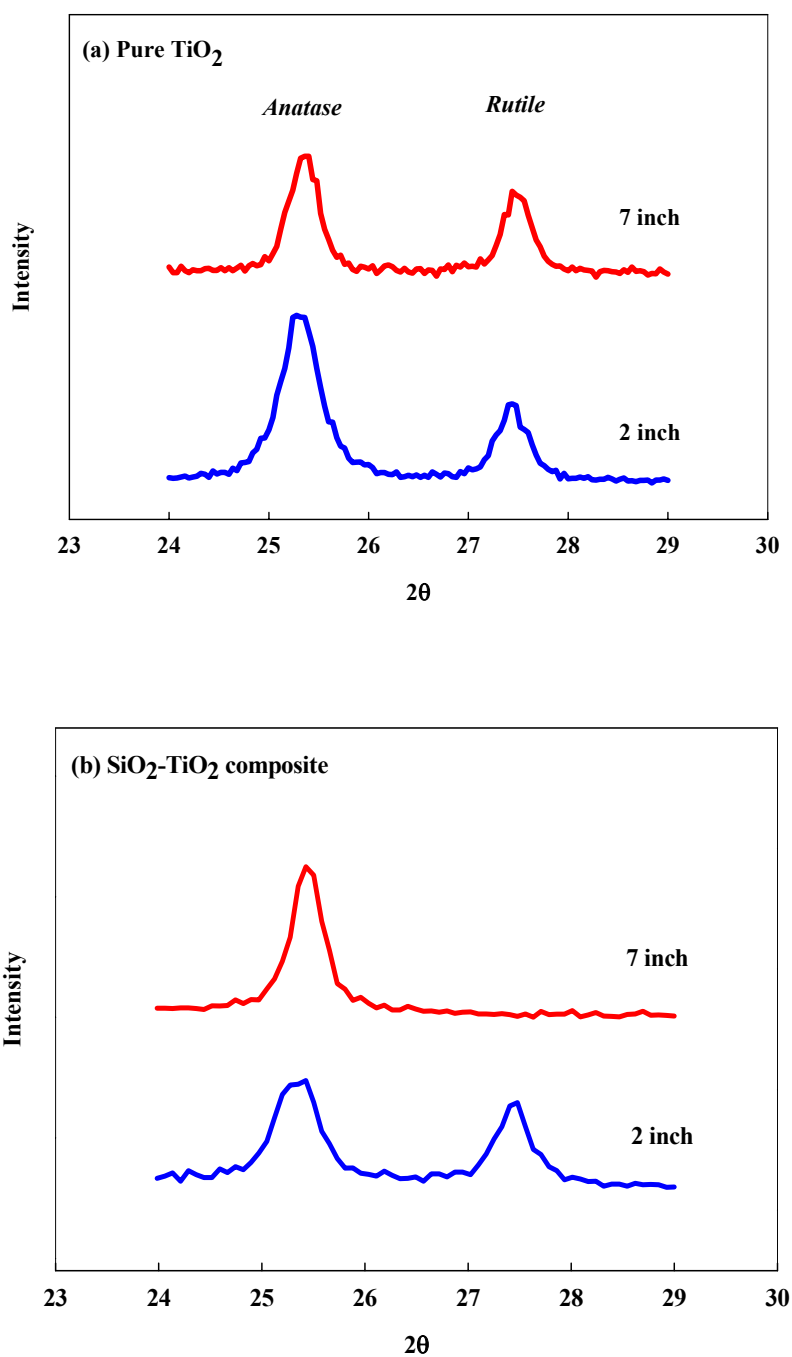


Figure 28 XRD patterns at low and high quench ring position for (a) pure TiO_2 (b) SiO_2 - TiO_2 composite.

2.1.3 Bonding analysis from FTIR

Figure 29 shows the FTIR spectra of the $\text{SiO}_2\text{-TiO}_2$ that are recorded in the spectral range of $4000\text{-}400\text{ cm}^{-1}$. It clearly shows that Si-O-Ti bonding is found for all samples at any Si:Ti molar ratio and quench ring position according to chemical bonding from FTIR analysis (Pickup *et al.*, 1999; Tartaj *et al.*, 2001) as shown in Table 15. Figure 29a indicated that when Si:Ti ratio increased, Si-O-Ti vibration band shifted closer to the that of Si-O-Si symmetric stretching of SiO_2 . The peak intensities near 1180 cm^{-1} and 476 cm^{-1} increase with increasing SiO_2 content, while the peak intensities near 400 cm^{-1} decrease. The appearance of the Si-O-Ti peaks indicates that $\text{SiO}_2\text{-TiO}_2$ nanocomposite material was obtained.

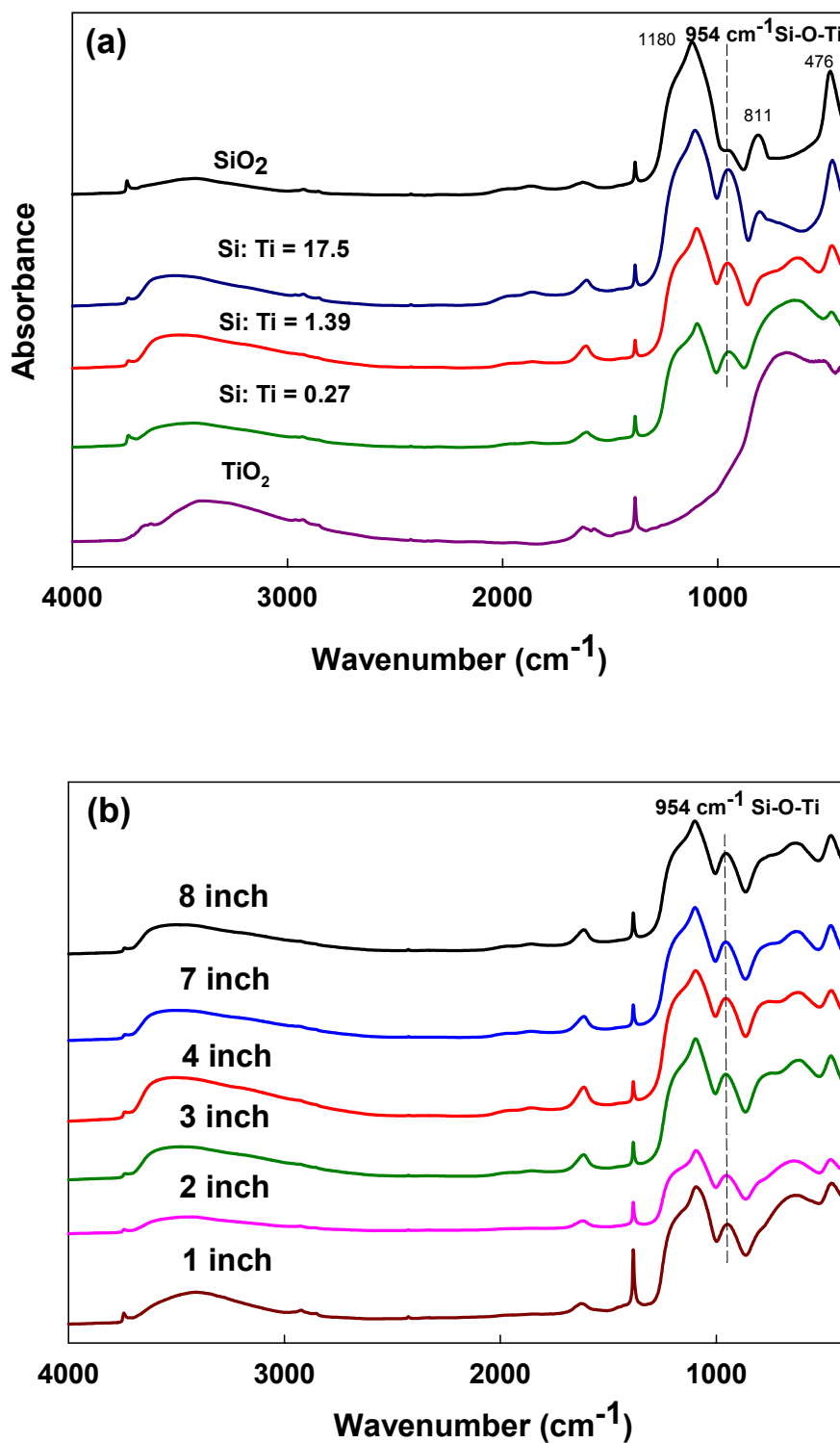


Figure 29 FTIR spectra of SiO_2 - TiO_2 (a) with different silica content (b) with different quench ring position.

Table 15 Chemical bonding from FTIR analysis.

Bonding	Peak position (cm ⁻¹)
Si-O-Si asymmetric stretching	1180
Si-O-Si symmetric stretching	811
Si-O-Si bending	476
Ti-O	400
Ti-O-Ti	775
Al-O (AlO ₄)	830
Al-O (AlO ₆)	530-680
Si-O-Ti	954-965
Si-O-Al	1056-1074
Si-OH and adsorbed water	3600-3000
H-O-H bending	1610

Source: Pickup *et al.* (1999); Tartaj *et al.* (2001); Baranwal *et al.* (2001); Mendoza-Serna *et al.* (2002)

2.1.4 Zeta potential for SiO₂-TiO₂ composite

SiO₂-TiO₂ nanocomposite has more negative zeta potential value which is lower than pure TiO₂ for a given pH. Figure 30 presents changes of zeta potential of SiO₂-TiO₂ nanocomposite particles in aqueous suspensions as a function of pH. The results show that the zeta potential of SiO₂-TiO₂ is lower than -30 mV in the pH range from 6 to 10. This clearly confirmed good dispersion of nanocomposite in water. It can be seen that the electrophoresis behavior of SiO₂-TiO₂ system is considerably affected by different morphology at both high and low quench ring position, compared to pure TiO₂ and pure SiO₂. Pure TiO₂ and pure SiO₂ exhibit an isoelectric point (IEP) at about pH 4.5 and pH 2, respectively. When adding SiO₂ to form SiO₂-TiO₂ nanocomposite, the electrophoresis curve was shifted toward the acidic region. The corresponding IEPs were shifted to about 2.8 and 2.6 for SiO₂-

TiO₂ at quench ring position of 7 and 2 inch, respectively. Consequently, the deposition of SiO₂ on TiO₂ changed surface charge characteristics significantly. In conclusion, SiO₂-TiO₂ nanocomposite is better dispersion than pure TiO₂ which is a result of more surface charge of SiO₂-TiO₂ confirmed by zeta potential.

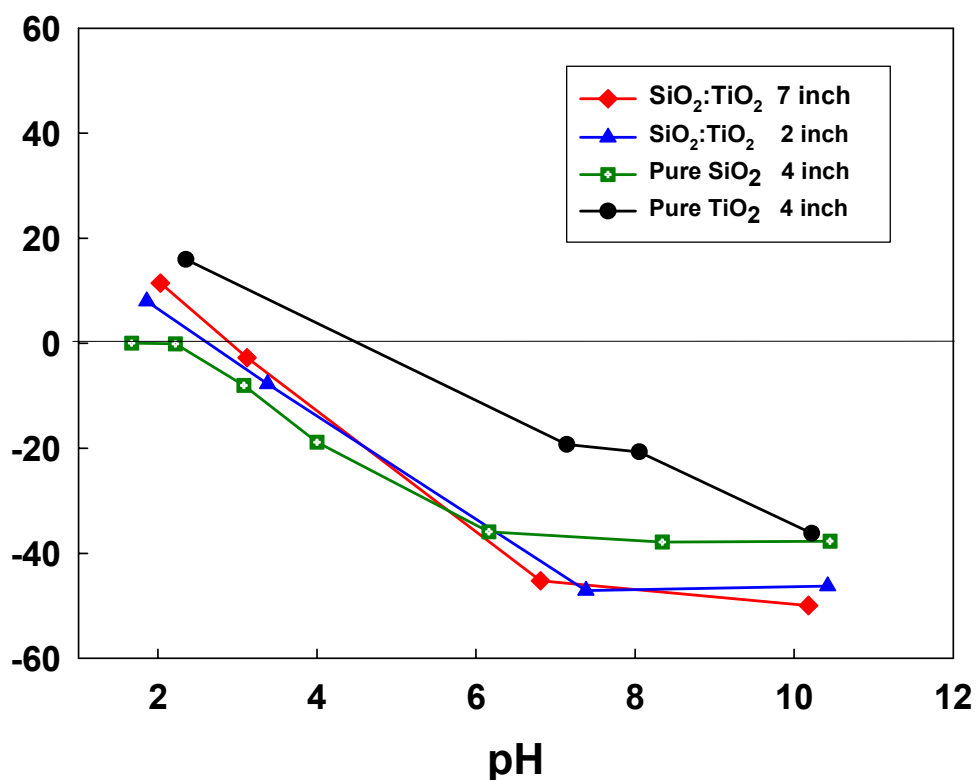


Figure 30 Zeta potential of SiO₂-TiO₂ composite as a function of pH for different quench ring position.

2.2 SiO₂-Al₂O₃ System

2.2.1 Effect of Si:Al molar ratio

According to the SiO₂-TiO₂ results, the addition of secondary material into an oxide can control phase transitions. The Si:Al precursor concentration mole ratio was examined from 0.6 to 66 for nanocomposite material compared to pure SiO₂ and pure Al₂O₃. The effect of TEOS concentration ranging

from 2.06×10^{-5} to 2.31×10^{-3} mol/L (Table 16) was studied by changing the evaporating temperature of TEOS while that of the ATSB precursor was kept constant. SiO₂ produced is amorphous corresponding to X-ray diffraction results. It is known, however, that some variations in crystal structure can occur depending on the precursor used (Hayashi *et al.*, 1997). Under the conditions studied in this work, mainly γ -phase of pure Al₂O₃ was mainly produced by decomposition of 10 mol% of ATSB in sec-butanol.

Table 16 Specific surface area and particle size variation for different Si and Al precursor feed rates.

No.	Precursor molar ratio	Phase composition ¹	SSA ² (m ² /g)	dp ² (nm)
1	SiO ₂	Amorphous SiO ₂	262.28	8.8
2	Si:Al = 66	Amorphous SiO ₂	93.19	24.5
3	Si:Al = 48	Amorphous SiO ₂	-	-
4	Si:Al = 30	Amorphous SiO ₂	-	-
5	Si:Al = 24	Amorphous SiO ₂	92.23	24.2
6	Si:Al = 2	Amorphous+ γ -Al ₂ O ₃	79.04	24.1
7	Si:Al = 1.4	Amorphous+ γ -Al ₂ O ₃	-	-
8	Si:Al = 0.6	Amorphous+ γ -Al ₂ O ₃	72.73	23.9
9	Al ₂ O ₃	γ -Al ₂ O ₃ + unidentified	46.28	35

¹ From XRD

² From BET, multiple point

As shown in Figure 31, when SiO₂ precursor content increases, Al₂O₃ peaks decreases in intensity and completely disappeared when Si:Al precursor molar ratio was 24. However, the results from energy dispersive X-ray spectroscopy (Appendix D) still have all elements of Si, Al and O for all SiO₂-Al₂O₃ nanocomposites. These results indicated that the addition of SiO₂ can suppress γ -

Al_2O_3 phase. When the Si:Al ratio was increased to 24, XRD patterns showed only amorphous SiO_2 and no Al_2O_3 peak was observed. However, the addition of SiO_2 precursor only slightly increases specific surface area of SiO_2 - Al_2O_3 nanostructured composite as shown in Table 16. Therefore, the main effect for SiO_2 content is on the crystal phase of nanocomposite material (Figure 31).

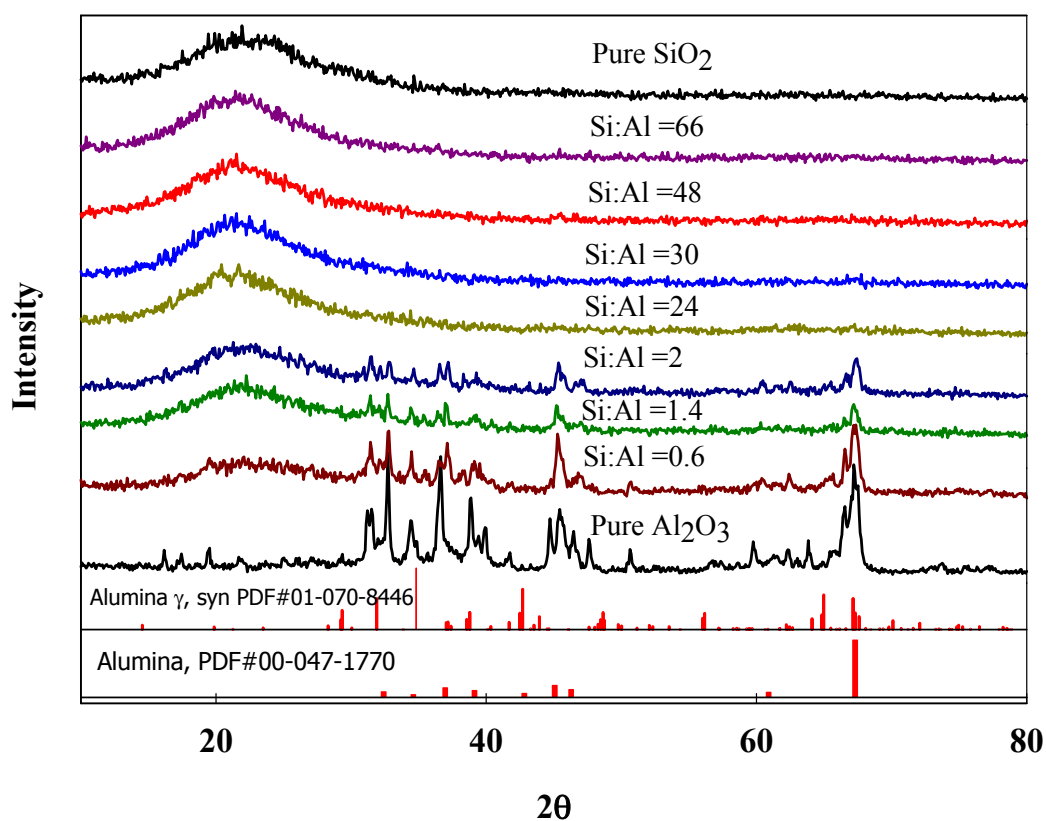


Figure 31 XRD patterns of composite SiO_2 - Al_2O_3 powder produced at different precursor molar ratios.

2.2.2 Effect of quench ring position of $\text{SiO}_2\text{-Al}_2\text{O}_3$ on specific surface area and morphology

It is similar to $\text{SiO}_2\text{-TiO}_2$ system for the effect of quench ring position on specific surface area. Decreasing quench ring location while Si:Al precursor molar ratio was controlled at 2, specific surface area increased and smaller d_{BET} was obtained (Figure 32). This is due to shorter residence time and incompleteness of sintering/coalescence of SiO_2 and Al_2O_3 .

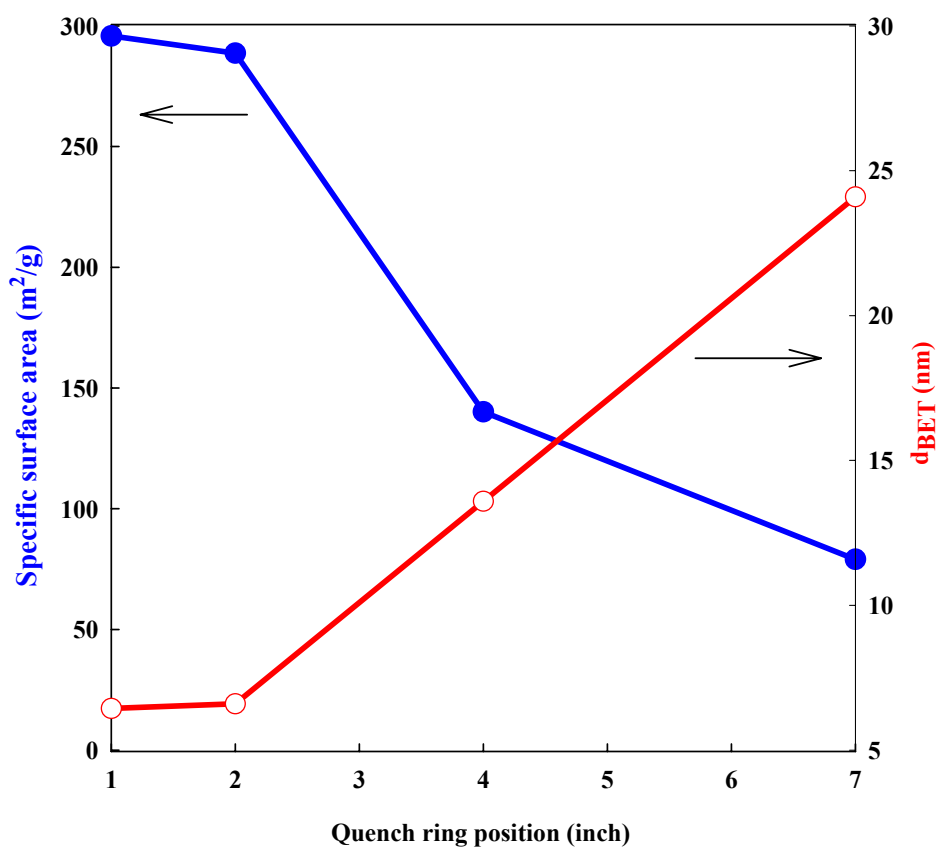


Figure 32 Specific surface area and particle size of $\text{SiO}_2\text{-Al}_2\text{O}_3$ as a function of quench ring position (at precursor molar ratio Si:Al = 2) for a CH_4 flowrate of 1 lpm.

Interestingly, morphology of $\text{SiO}_2\text{-Al}_2\text{O}_3$ system is different from that of $\text{SiO}_2\text{-TiO}_2$ system. This $\text{SiO}_2\text{-Al}_2\text{O}_3$ system showed only solid mixture or solid solution of nanocomposite because of the presence of an atom with ionic radius of Si^{4+} (0.40 Å) (Vemury and Pratsinis, 1995) similar to Al^{3+} (0.53 Å) (Vemury and Pratsinis, 1995). Si^{4+} can substitute for Al^{3+} in Al_2O_3 and form a substitutional solid solution. The ATSB and TEOS precursors vapor decomposes to Al_2O_3 and SiO_2 , respectively, which then formed a mixture of $\text{SiO}_2\text{-Al}_2\text{O}_3$ nanocomposite as shown in Figure 33. In this process, ATSB decomposed to produce supersaturated aluminum oxide vapor followed by the formation of primary alumina particles by homogeneous nucleation which then further grew by the condensation of vapor molecules (Moravec and Smolik, 2001). Therefore, it is reasonable to predict the formation mechanism of $\text{SiO}_2\text{-Al}_2\text{O}_3$ nanocomposite following the same path in the co-flow diffusion flame used as shown in Figure 33a.

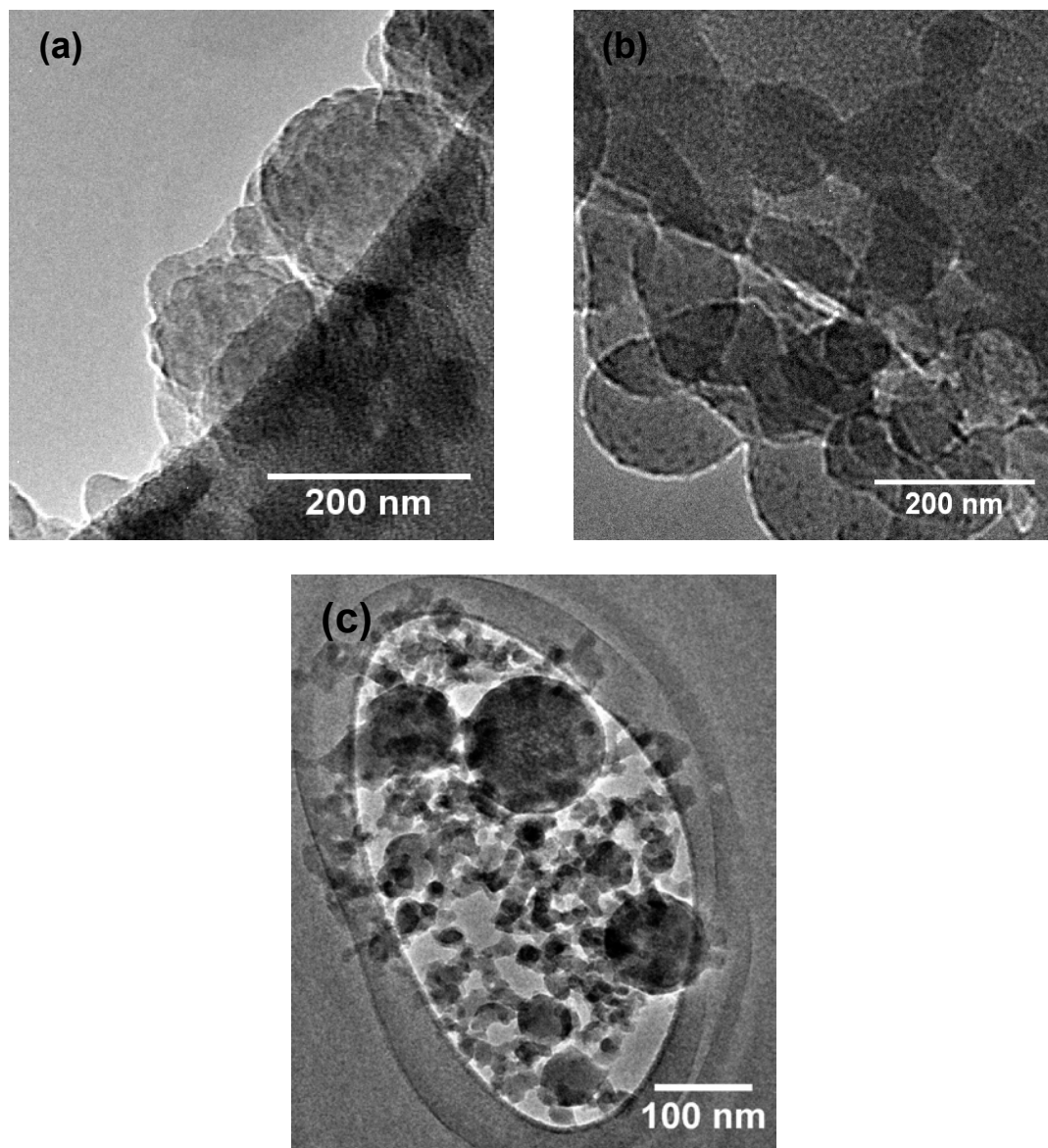


Figure 33 TEM images of $\text{SiO}_2\text{-Al}_2\text{O}_3$ composites prepared at different conditions
(a) quench ring position of 4 inch, precursor molar ratio of Si:Al = 0.6
(b) quench ring position of 4 inch, precursor molar ratio of Si:Al = 66 (c)
quench ring position of 2 inch, precursor molar ratio of Si:Al = 2.

2.2.3 Chemical vibration bonding from FTIR of SiO₂-Al₂O₃ system

The appearance of the Si-O-Al peaks from FTIR-spectra (Figure 34) indicates that SiO₂-Al₂O₃ nanocomposite material was obtained according to chemical bonding in Table 15. Figure 34a clearly show that Al-O (AlO₄) and Al-O (AlO₆) bondings are found for Al₂O₃ (Baranwal *et al.*, 2001). In this study, SiO₂-Al₂O₃ nanocomposite material showed Si-O-Al bond vibration in the range of 1054-1112 cm⁻¹ for all samples at any Si:Al ratio and quench ring position according to the results from other researchers that was detected by FTIR in the range of 1056-1074 cm⁻¹ (Mendoza-Serna *et al.*, 2002). It indicated that when Si:Al ratio increased, the Si-O-Al vibration band shifted closer to that of Si-O-Si symmetric stretching of SiO₂ (Figure 34a). The peak intensities near 1180 cm⁻¹ and 476 cm⁻¹ increase with increasing SiO₂ content, while the peak intensities near 830 cm⁻¹ decrease. In conclusion, Si-O-Al bonding is existed for synthesized SiO₂-Al₂O₃ nanocomposite material.

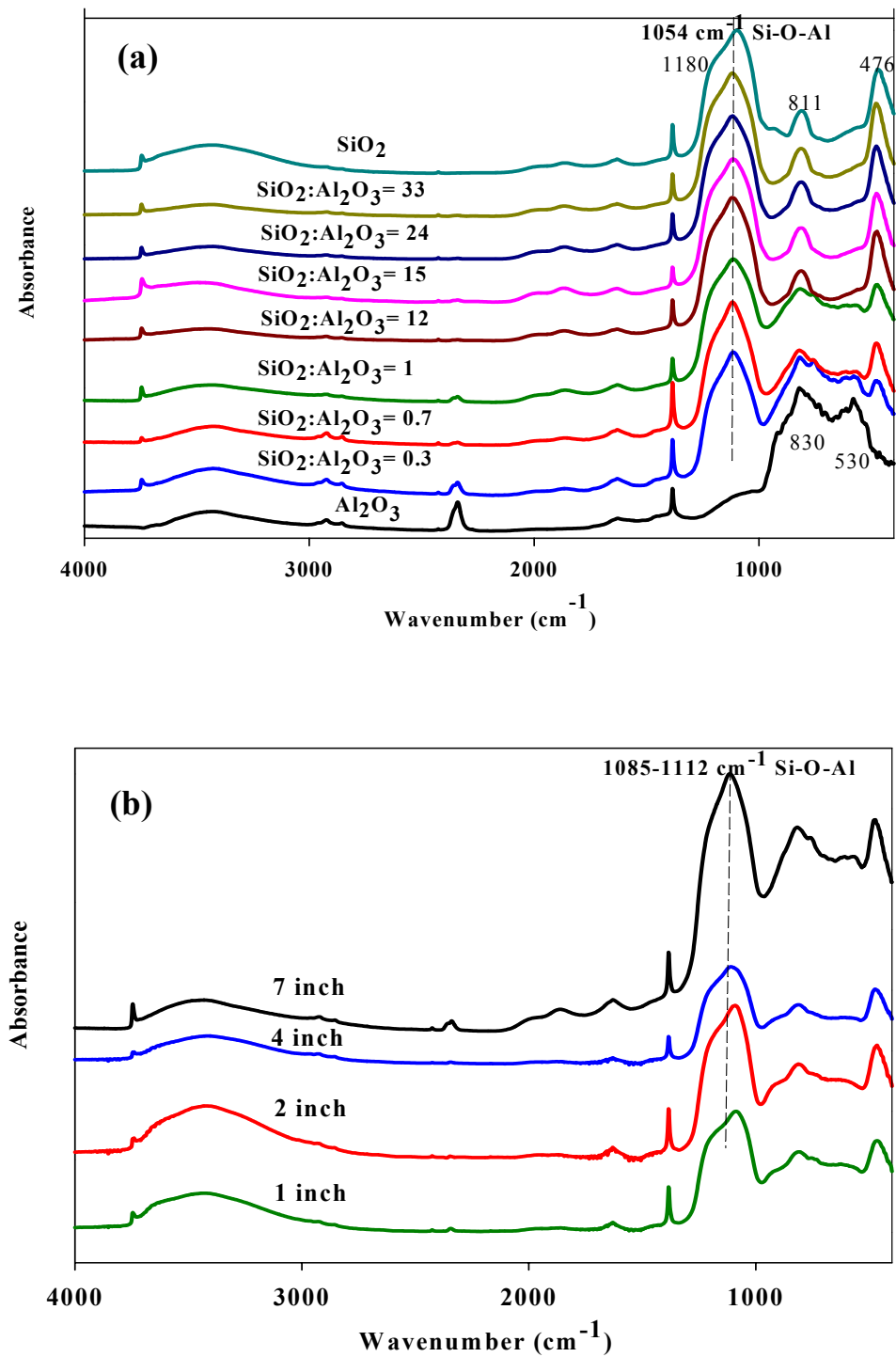


Figure 34 FTIR spectra of $\text{SiO}_2\text{-Al}_2\text{O}_3$ (a) with different silica content and (b) with different quench ring position.

2.2.4 Zeta potential for SiO₂-Al₂O₃ composite

SiO₂-Al₂O₃ nanocomposite has more negative zeta potential when compared to pure SiO₂ or Al₂O₃ at a given pH. Figure 35 shows changes of zeta potential of SiO₂-Al₂O₃ nanocomposite particles in aqueous suspensions as a function of pH. It can be seen that the electrophoresis behavior is considerably affected by different morphology at high and low quench ring position when compared to pure TiO₂ and pure SiO₂. Pure Al₂O₃ and pure SiO₂ exhibit an isoelectric point (IEP) at about pH 7.2 and pH 2, respectively. When adding SiO₂ to form SiO₂-Al₂O₃ nanocomposite, the electrophoresis curve was shifted toward the acidic region. Therefore, the mixture solid solution of SiO₂-Al₂O₃ change surface charge characteristics. In conclusion, SiO₂-Al₂O₃ nanocomposite is more stable than single component of SiO₂ or Al₂O₃ which is a result of more surface charge by zeta potential. This gives added strength to the end product for ceramic applications when a high zeta potential is obtained and it can be ensure that the particles are densely packed.

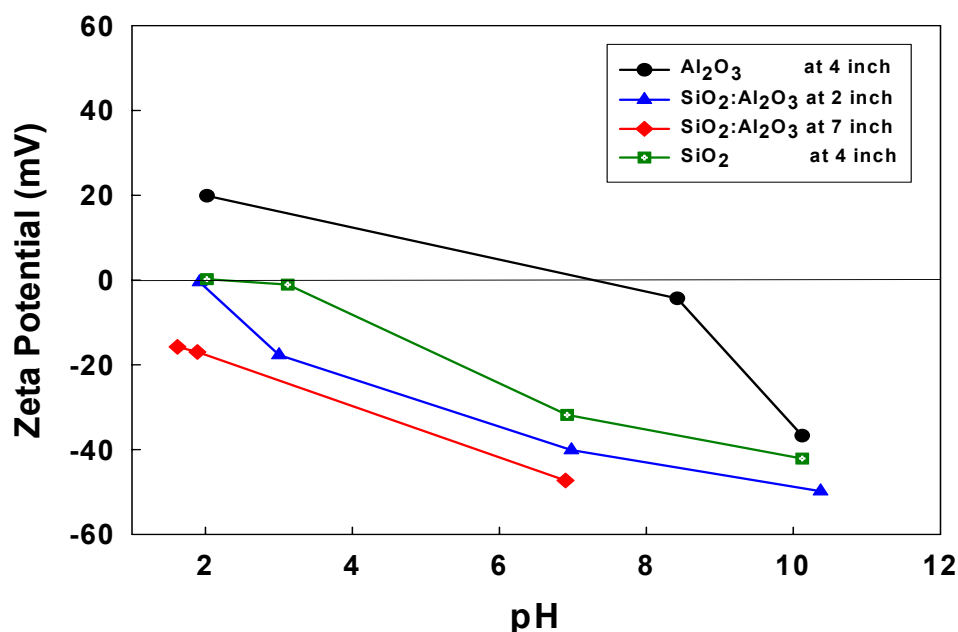


Figure 35 Zeta potential of SiO₂-Al₂O₃ composite as a function of pH for different quench ring position.

3. Part III: Mercury Capture Using Differential Bed Reactor

3.1 Kinetic Reaction Model

A qualitative mechanism for the capture of mercury on TiO₂ sorbent using UV irradiation has been proposed (Wu *et al.*, 1998). On irradiating with UV light, active sites of sorbent become available wherein surface generated hydroxyl radicals and the absorbed mercury can react to form a complex with sorbents. In this study, it was assumed that mercury capture with UV irradiation occurred by 2 mechanisms: simple adsorption on the UV unexposed surfaces (equation 1) and UV assisted adsorption on the UV exposed surfaces (equation 2).



S represents the sorbent active site. The rate of the Hg capture can be written in a general form as

$$\frac{dx}{dt} = kA_s^n C_{\text{Hg}}^\alpha \quad (3)$$

where x = fraction of sorbent that is associated with the mercury species

$$= \frac{\text{mole Hg adsorbed}|_t}{\text{mole Hg adsorbed}|_{\text{saturation}}} = \frac{\text{surface area occupied by Hg}}{\text{total initial surface area}} \quad (4)$$

k = rate constant

A_s = number of vacant active sites or available surface area for Hg capture
 $= S_0(1-x)$; (m²/g)

S_0 = initial specific surface area of sorbent (m²/g)

C_{Hg} = concentration of mercury in the gas phase (μg/m³)

n, α = fitting parameters obtained from experiments

It was assumed that the total surface area of the sorbent obtained from N₂ adsorption (S_0) was available for mercury adsorption. However, it should be remarked that this assumption may lead to some errors because Hg molecule (atomic radius 1.6 Å) is bigger than N₂ molecule (atomic radius 0.55 Å) (Dean, 1985), therefore Hg molecules can not be adsorbed with in some narrow pores. All active sites were also assumed to have equal binding energy for irreversible monolayer adsorption. Then, the amount of adsorbed Hg at saturation point was calculated by equation 5,

$$\begin{aligned} \text{mole Hg adsorbed} \Big|_{\text{saturation}} &= \frac{(S_0)(\text{mass of sorbent})}{(\text{projected area of Hg molecule})(N_0)} \\ &= \frac{(S_0(m^2/g) * \text{mass of sorbent}(g))}{(1.02 \times 10^{-19} \text{ m}^2/\text{molecule} * 6.023 \times 10^{23} \text{ molecules/mole})} \quad (5) \end{aligned}$$

The n and α show the influence degree and sensibility of corresponding variables (i.e., active sites and Hg concentration) on the capture rate, comparatively. If n and α are found to be unity, it reveals that the above mechanisms are elementary steps (following stoichiometric relation in the proposed mechanisms) (Levenspiel, 1999). Due to the sorbents are nanostructures, the internal diffusion resistance can be neglected; consequently, n is assumed to be 1 (Mahuli *et al.*, 1997; Lee *et al.*, 2004). Then, from equation 3 the initial rate of Hg capture is

$$\left. \frac{dx}{dt} \right|_{t \rightarrow 0} = kS_0(1-x)C_{Hg}^\alpha \Big|_{t \rightarrow 0} \approx kS_0(1-x)C_{Hg,0}^\alpha \quad (6)$$

where $C_{Hg,0}^\alpha$ = inlet concentration of Hg in gas phase ($\mu\text{g}/\text{m}^3$)

After integrating the rate for a short period of time (Δt), it gives the following:

$$-\ln(1-x) = kS_0C_{Hg,0}^\alpha \Delta t \quad (7)$$

and

$$-\ln(1-x) = KC_{Hg,0}^\alpha \quad (8)$$

where $K = kS_0\Delta t$

By varying the inlet Hg concentration, the parameter α and the initial rate constant k ($\mu\text{g}^{1-\alpha} \text{m}^{3\alpha-2} \text{s}^{-1}$) were determined from a plot between $-\ln(1-x)$ and $C_{\text{Hg},0}$ on a log-log scale.

3.2 Sorbent Physical Properties

The physical properties of the commercial and laboratory synthesized sorbents used in this study are shown in Table 17. Sorbent particle size ranged from 70 nm to 3.3 μm and specific surface areas ranged from 14.3 to 390.6 m^2/g .

Table 17 Properties of various sorbents used for the mercury capture experiments.

No.	Type of sorbent	Chemical Formula	Crystalline phase/Type	Particle size ¹ (nm)	BET surface area (m ² /g)	
					Measured	Manufacturer specified
1	Iron Oxide Red	α -Fe ₂ O ₃	Hematite	70	21.2	20
2	Trans Oxide Yellow	α -FeOOH	Goethite	90x210	138.9	104
3	Trans Oxide Red	α -Fe ₂ O ₃ / γ -Fe ₂ O ₃	Hematite / Maghemite	30x120	127.4	117
4	Trans Oxide Brown	α -Fe ₂ O ₃ / MnFe ₂ O ₄	Hematite / Manganese iron oxide	30x120	96.9	90
5	Titanium Dioxide	TiO ₂	Anatase / Rutile	60	61.8	50
6	Titania Pillared Interlayered Clays (TiO ₂ -PILC)	(TiO ₂) _{0.68} (Si _{3.99} Al _{1.92})(Mg _{1.73})O ₁₀ (OH) ₂	Andalusite/Anatase	0.6x1.5 μ m	14.3	NA
7	Synthetic SUZ-4 zeolite	K ₅ Al ₅ Si ₃₁ O ₇₂	Zeolite	0.3x4 μ m	390.6	NA
8	Synthetic magnetite	Fe ₃ O ₄	Magnetite	1x3.3 μ m	109.2	NA

¹ From SEM (two dimensions are width by length for non-spherical particle)

Scanning electron microscopy (SEM) images of each sorbent is shown in Figure 36. Each sorbent has a different morphology depending on its crystal structure and method of synthesis. For example, titania pillared clays have a plate-like morphology (Figure 36f), SUZ-4 zeolite particles are needle-like structure (Figure 36g) having micropores with the pore width of 5.8 Å determined by using a Saito-Foley (SF) pore size distribution peak model, and magnetite Fe_3O_4 particles are acicular crystals (Figure 36h). The crystal phase of each sorbent was determined by XRD. The XRD pattern of TiO_2 indicates that it is a mixture of anatase and rutile; the TiO_2 -PILC is primarily composed of the anatase and a mineral like andalusite; and Trans Oxide Brown consists of hematite and a complex structure of Mn (α - $\text{Fe}_2\text{O}_3/\text{MnFe}_2\text{O}_4$).

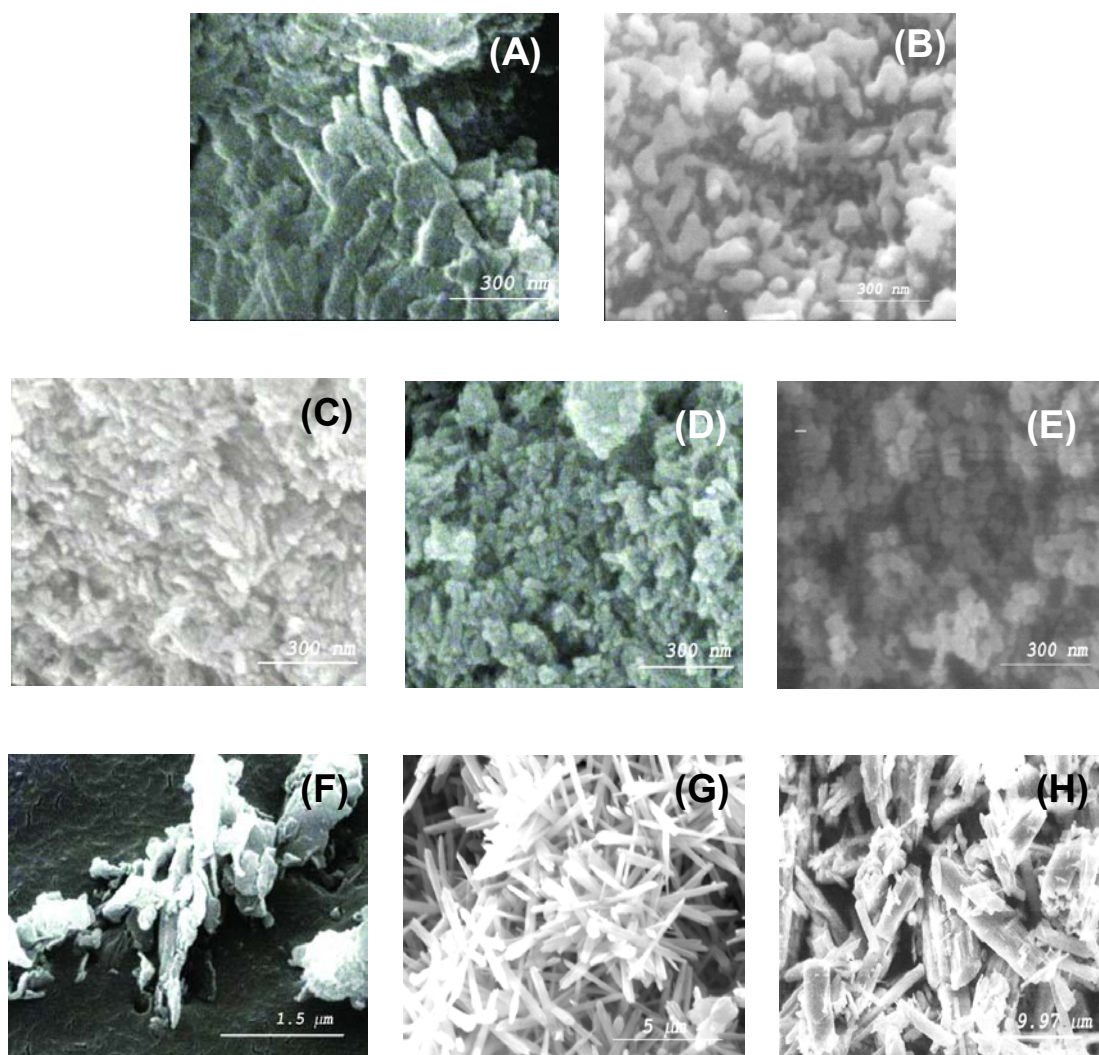


Figure 36 SEM images of (a) Iron Oxide Red (b) Trans Oxide Yellow (c) Trans Oxide Red (d) Trans Oxide Brown (e) TiO_2 (f) titania PILC (g) synthetic SUZ-4 zeolite (h) synthetic Fe_3O_4 magnetite.

3.3 Mercury Capture Efficiency

The mercury capture efficiency of various sorbents for an inlet concentration of $75 \pm 1.9 \mu\text{g}/\text{m}^3$ is shown in Figure 37. Four sorbents, Trans Oxide Brown, TiO_2 , TiO_2 PILC, and SUZ-4 zeolite, had mercury capture efficiencies greater than 70% with UV irradiation. TiO_2 had the highest efficiency (~89 %) with UV

irradiation. They also showed high efficiency for an inlet concentration of $610 \pm 8.6 \mu\text{g}/\text{m}^3$ with UV irradiation while synthetic Fe_3O_4 magnetite was not shown as good sorbent for this concentration. The mercury capture efficiency by nanostructured sorbents in the presence of UV is not only a function of accessible active sites but also of photocatalytic activity. Thus, the capture efficiency is depended on a combination of physical (morphology and size) and chemical (crystalline phase) properties of the sorbents (De Lasa *et al.*, 2005).

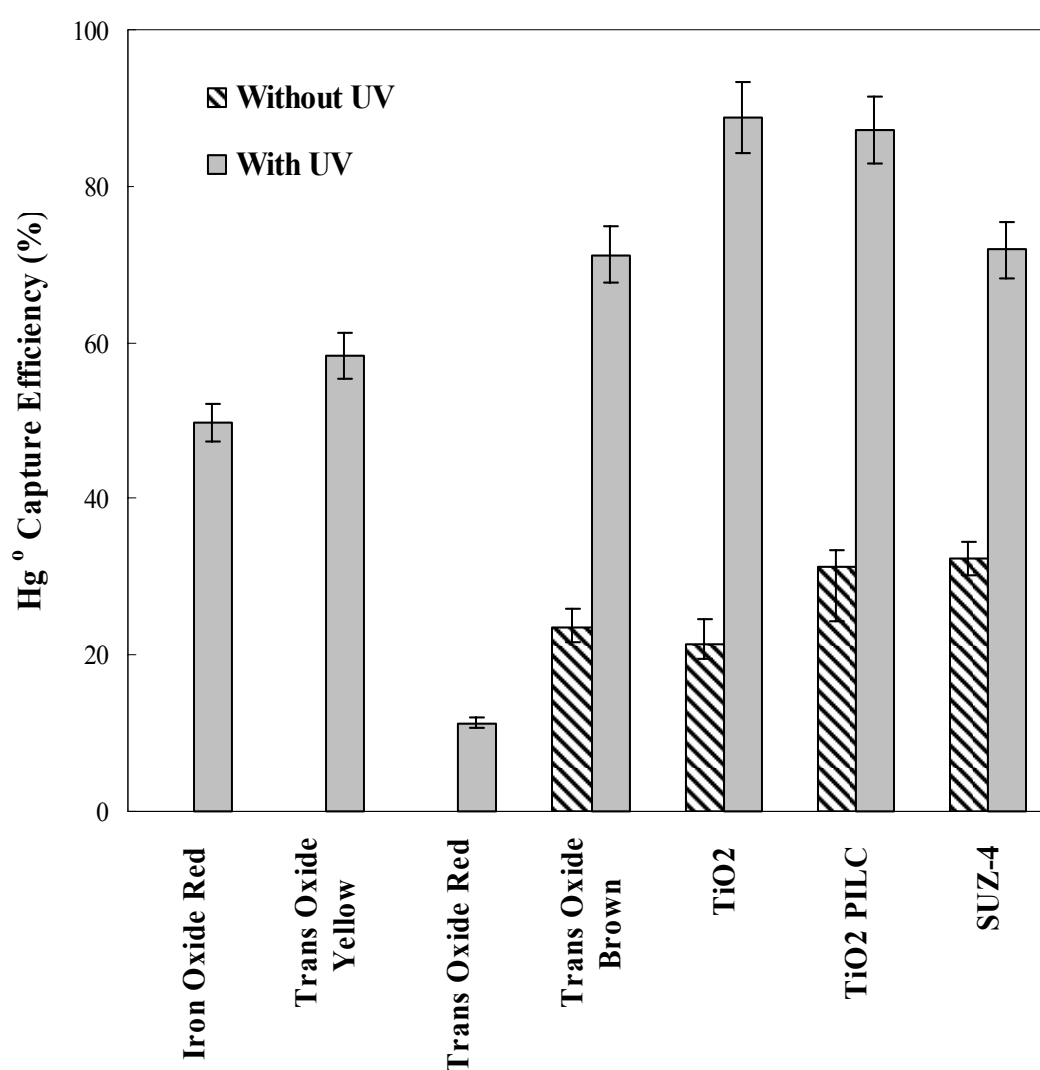


Figure 37 Hg^0 capture efficiency in differential bed reactor for an inlet Hg concentration of $75 \pm 1.9 \mu\text{g}/\text{m}^3$ (with/without UV).

A key step in the capture of the mercury species is photocatalytic oxidation on the surface of the sorbent. This experiment shows that TiO_2 is superior to other sorbents for mercury capture in the presence of UV because of its superior photocatalytic property. It generates hydroxyl radicals ($\text{OH}\cdot$) effectively upon absorption of UV light (De Lasa *et al.*, 2005), which promotes HgO formation (Wu *et al.*, 1998). The crystalline phase affects the activity of a sorbent. The anatase phase of TiO_2 is more photoactive than the rutile phase (De Lasa *et al.*, 2005). The superior activity of TiO_2 belongs to the anatase phase as mentioned earlier. The mercury capture capability of SUZ-4 zeolite is influenced by the presence of a large number of adsorption sites. The surface area of the sorbent is an important factor in its overall reactivity and adsorption capacity. The surface area and pore structure of zeolite play important roles in catalytic activity of the sorbent. The pore size distribution of SUZ-4 zeolite indicates peak pore dimensions of 5.8 Å, which are larger than the size of Hg molecule; hence it may adsorb Hg within its pores. SUZ-4 zeolite may attract the great deal of attention of photocatalytic properties according to the results. The basic properties of the zeolites have led to dramatic changes and modifications in the molecular motion as well as the reactivity of molecules within the zeolites (Anpo, 2000). TiO_2 -PILC is a nano-composite of pillared clay that acts as metal capturing groups and anatase phase of TiO_2 ; as a result, the ability of pillared clay for binding Hg ions is enhanced. However, TiO_2 -PILC had a lower efficiency than pure TiO_2 because of its much lower specific surface area. Concerning Trans Oxide Brown, an iron oxide containing hematite ($\alpha\text{-Fe}_2\text{O}_3$) and manganese complex (MnFe_2O_4), the photocatalytic mercury oxidation rate was observed to be the highest among the iron oxides. This is probably due to the presence of the manganese complex (MnFe_2O_4) that enhances the photocatalytic activity. However, further investigation should be conducted to identify the pathways and role of composition.

3.4 Initial Rate of Mercury Capture

DBR measurements were used to determine the kinetics of mercury capture for the four most effective sorbents TiO_2 , TiO_2 -PILC, SUZ-4 zeolite and

Trans Oxide Brown in the presence of UV irradiation. The initial rates of Hg capture per unit mass of sorbent at different Hg inlet concentrations with UV irradiation are summarized in Table 18. Initial rates were determined from DBR experiments conducted for 10 minutes with Hg inlet concentration ranging from 16 to 610 $\mu\text{g}/\text{m}^3$. As the Hg inlet concentration is increased, the initial rate of Hg uptake for each sorbent also increased confirming that adequate number of sites was available for these experiments. The maximum initial rate of Hg capture was observed for TiO_2 with an uptake rate of 13.5 $\mu\text{g Hg}/(\text{g sorbent}\cdot\text{min})$ for an inlet concentration of $610\pm 8.6 \mu\text{g}/\text{m}^3$.

Table 18 Initial rates of Hg capture for different Hg inlet concentrations with UV irradiation.

$C_{\text{Hg},0}$ ($\mu\text{g}/\text{m}^3$)	Initial rate of Hg uptake, $\frac{\mu\text{g Hg}}{(\text{g sorbent} \cdot \text{min})}$			
	TiO_2	TiO_2 PILC	Trans oxide brown	SUZ-4 zeolite
16	0.31	0.01	0.01	0.03
21	0.46	0.03	NA	0.02
45	0.59	0.05	0.04	0.06
75	1.83	0.21	0.33	0.32
610	13.45	1.30	1.59	1.70

Using equation (8), $-\ln(I-x)$ was plotted as a function of the Hg inlet concentration on log-log scale (Figure 38) and then α and k were determined from the slope and intercept, respectively.

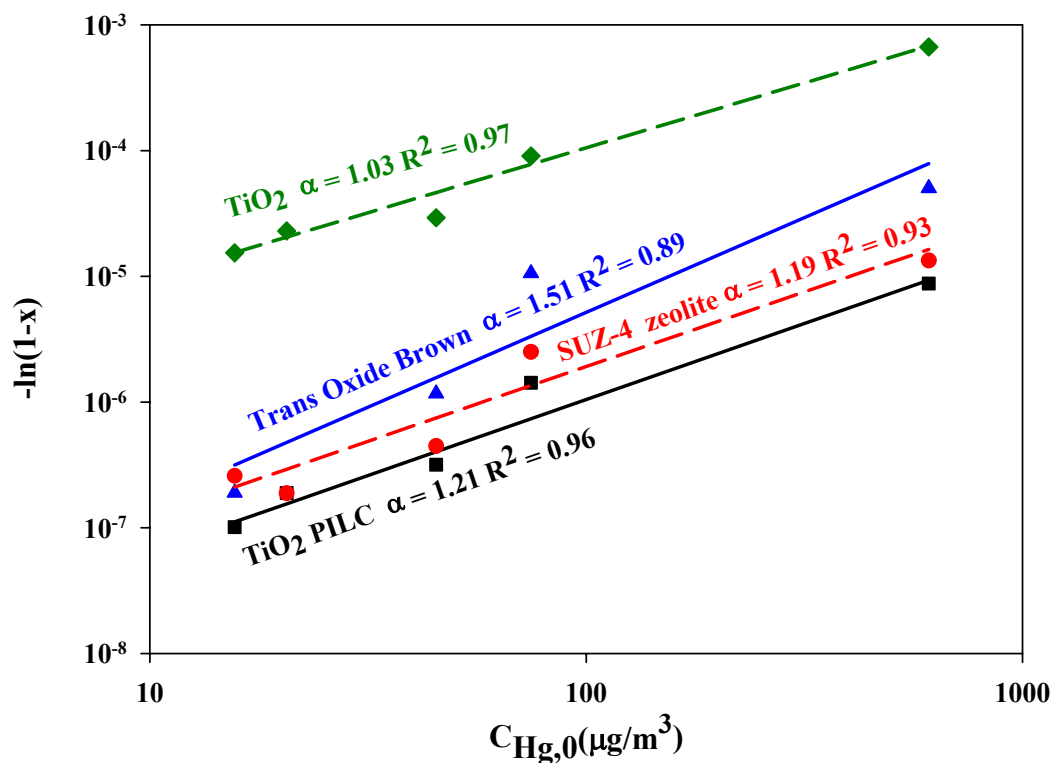


Figure 38 Log-log plot of conversion versus inlet mercury concentration to determine fitting parameter (α) and rate constant (k) The inlet Hg concentration was fixed at $75 \pm 1.9 \mu\text{g}/\text{m}^3$

(◆ TiO₂, ■ TiO₂ PILC, ● SUZ-4, ▲ Trans Oxide Brown).

As shown in Table 19, the value of α for each evaluated sorbent ranges from 1.03 to 1.51. The value of α for TiO₂ of 1.03, which agrees well with the value of 1.1 ± 0.1 for aerosol flow reactor, lower than the value (1.41) evaluated for the DBR system with previous measurements done (Lee *et al.*, 2004). The value of α shows the influence degree and sensibility of corresponding Hg concentration on the capture rate. The reaction rate constant (k) was found to range from 3.41×10^{-20} to $2.43 \times 10^{-17} \mu\text{g}^{1-\alpha} \text{m}^{3\alpha-2} \text{s}^{-1}$. The rate constant in a surface reaction controlling regime of the case of in situ generated TiO₂ particles, the reaction orders with respect to Hg concentration and UV intensity is shown and $k_{\text{exp}} = 1.84 \times 10^{-9} \exp(-1295.24/T) [(\text{m}^2/\text{g})^{-1}(\text{g}/\text{m}^3)^{-1}(\text{W}/\text{cm}^2)^{-0.39}(\text{sec})^{-1}]$ (Lee, 1999) or it is approximately $1.6 \times 10^{-18} \mu\text{g}^{1-\alpha}$

$\text{m}^{3\alpha-2} \text{s}^{-1}$, lower than the experiment in this research. This may be due to the system for sorbent feeding differs. The rate constant for TiO_2 is the highest among the tested sorbents primarily because of the superior photocatalytic activity. Though SUZ-4 zeolite has the largest surface area, it yielded low overall capture rate. This confirms that the photo-oxidation mechanism has the major contribution in the overall mercury capture.

Table 19 Summary of estimated parameters for an Hg inlet Hg concentration of $75 \pm 1.9 \mu\text{g}/\text{m}^3$ with UV irradiation.

Type of sorbent	k ($\mu\text{g}^{1-\alpha} \text{m}^{3\alpha-2} \text{s}^{-1}$)	α
TiO_2	$2.43 \cdot 10^{-17}$	1.03
TiO_2 PILC	$4.66 \cdot 10^{-19}$	1.21
Trans Oxide Brown	$8.6 \cdot 10^{-20}$	1.51
SUZ-4 zeolite	$3.41 \cdot 10^{-20}$	1.19

3.5 Sequential Extraction and Complete Digestion

As shown in Table 20, the three-step sequential extraction established that mercury associated with TiO_2 , TiO_2 PILC, and SUZ-4 zeolite was extracted almost entirely in the residual step, while over half of the Hg associated with Trans Oxide Brown was extracted in the surface bound step. These results indicate that the mercury associated with TiO_2 , TiO_2 PILC, and SUZ-4 zeolite is bound very strongly and is unlikely to leach from the sorbent under most environmental conditions. The strength of the bonds of Hg to the surfaces of the TiO_2 , TiO_2 PILC, and SUZ-4 zeolite may be enhanced by more complete oxidation of Hg^0 to HgO at the TiO_2 or zeolite surface under UV irradiation (Wu *et al.*, 1998). The mercury extracted from the Trans Oxide Brown by the ion exchangeable solution may be adsorbed to the iron oxide surface (e.g., $\equiv\text{Fe-O-Hg}^+$) by weaker bonds than those of dissolved Hg-NH_3 complexes (Noel *et al.*, 2007). Gaseous oxidation of Hg^0 to HgO can occur in the presence of UV (Haidouti, 1997; Granite *et al.*, 1999; Granite and Pennline, 2002).

The gaseous HgO may interact differently with the iron oxide. For the Trans Oxide Brown, Hg⁰ oxidation may occur in the gas phase, not directly on the sorbent surface.

Mercury that was not mobilized in either of the first two steps of the sequential extraction was extracted by completely dissolving the sorbent in concentrated acids. The sum of the mercury extracted in the three individual steps was within 2×10^{-6} g/g of the total mercury content determined through a single step complete digestion. For the TiO₂ PILC and SUZ-4 zeolite, the single step measurement provided a higher value than the sum from the three extracts, which may be explained by the potential loss of mercury during the multiple transfer steps in the sequential extraction process. These two extraction processes show the similar result as the estimate based on the concentration differences between the inlet and outlet gas phase mercury integrated over the reaction duration time (Table 20).

Table 20 Percentage of mercury extracted at different steps of the sequential extraction study and total solid phase Hg concentration for an inlet concentration of $75 \pm 1.9 \mu\text{g}/\text{m}^3$.

Samples	Percent of Hg Mass Extracted			Solid-phase Hg Concentration ($\mu\text{g Hg}/\text{g sorbent}$) ¹		
	Exchangeable	Acid Soluble	Residual Solid	Sequential extraction ²	Completion digestion ³	Downstream of DBR ⁴
Trans Oxide Brown	73	BDL	27	4.87	4.18	3.34
TiO ₂	BDL	BDL	100	11.00	12.42	18.28
TiO ₂ PILC	BDL	BDL	100	2.08	2.99	2.11
SUZ-4 zeolite	BDL	BDL	100	4.01	6.63	3.19

BDL = Below Detection Limit.

¹ For a reactor running time of 10 minutes

² Concentration was calculated by adding the total amount of Hg extracted in each of the three steps of the sequential extraction procedure.

³ Concentration was calculated by a one step complete digestion of the sorbent using concentrated acids at high temperature and pressure.

⁴ Concentration was calculated from the difference in the inlet and outlet gas phase mercury concentration over 10 minutes of reactor operation.

4. Part IV: Photocatalytic Degradation of Methyl Orange Dye

The absorbance of dye solutions before and after methyl orange degradation was measured at different degradation times. Figure 39 shows UV-vis absorption intensity at 460 nm of pure TiO_2 and different Si:Ti ratios nanoparticles containing methyl orange as a function of time. It is observed that the addition of SiO_2 to TiO_2 can suppress its photocatalytic activity of methyl orange dye according to the results of Park *et al.* (2004).

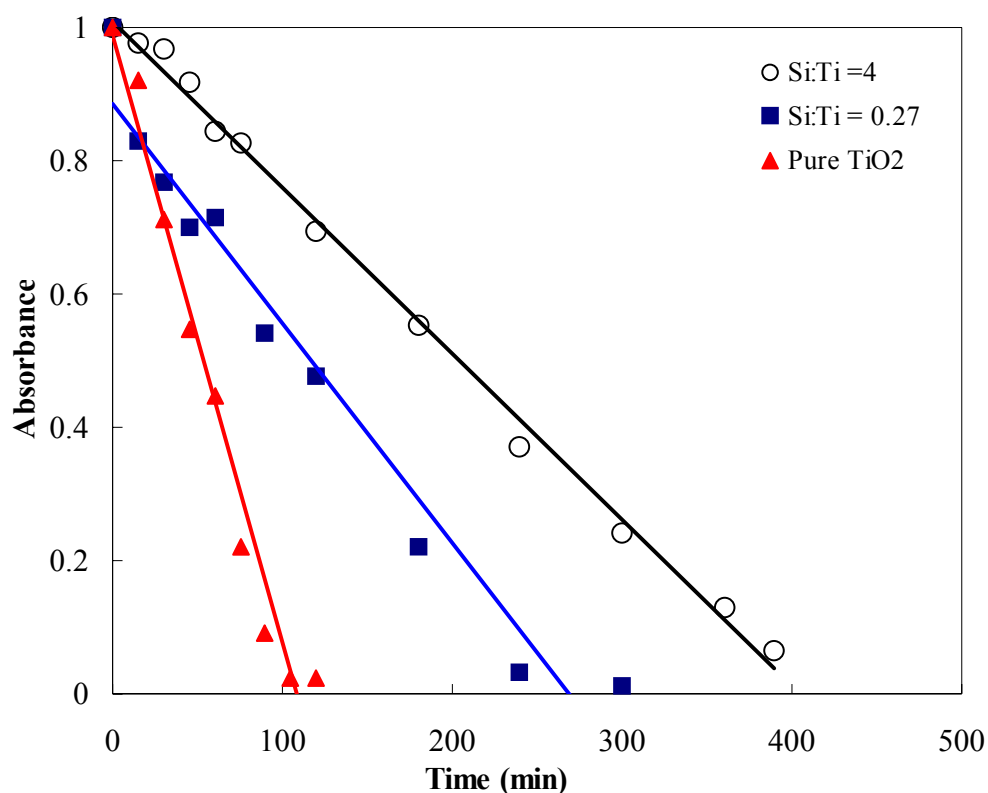


Figure 39 UV-vis absorption intensity at 460 nm for photocatalytic degradation of methyl orange of pure TiO_2 and different Si:Ti ratio at 4 inch quench position.

As shown in Figure 38, it was found that methyl orange dye was also slightly photodegraded by silica-coated TiO_2 (Figure 27c) as a result at 2 inch position, in

contrast to the result obtained with pure TiO_2 that it can absorb rapidly with time. As the results for photocatalytic degradation with methyl orange dye (Figure 40) and zeta potential (Figure 30), it may use for pigment or cosmetic applications since SiO_2 coating can improve both the pigment durability and dispersion properties.

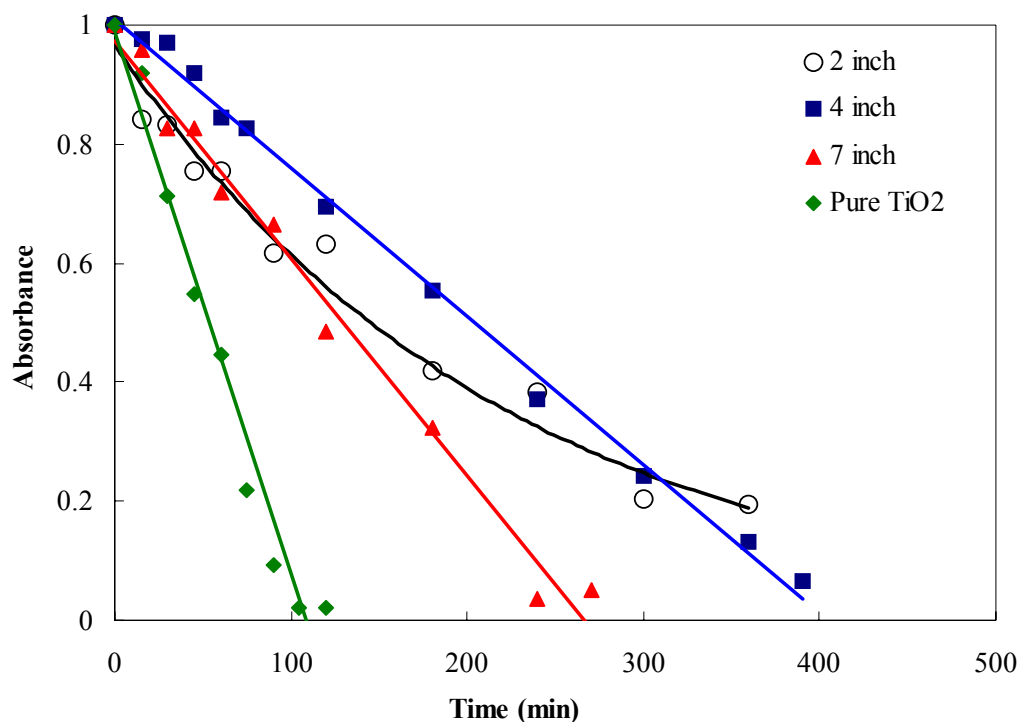


Figure 40 UV-vis absorption intensity at 460 nm for photocatalytic degradation of methyl orange of pure TiO_2 and different quench ring position at $\text{Si}:\text{Ti} = 4$.

Figure 41 shows UV-vis absorption intensity for photocatalytic inactivation of methyl orange solution for SUZ-4 zeolite and TiO_2 -PILC. This is due to aluminosilicate structure of both may shield and prevent oxidation of organic molecules. In addition, different conditions of 1 and 1.8 lpm CH_4 flowrate for TiO_2 synthesis by flame aerosol technique made different absorbance trend. It is observed that synthesized TiO_2 with 1.8 lpm CH_4 flowrate can be more photocatalytic with methyl orange solution than 1 lpm CH_4 flowrate as shown in Figure 41. This result was described that photocatalytic depends on condition of synthesis to get more different % anatase of TiO_2 that affected on its photocatalytic. However, for this

experiment, commercial TiO_2 (P25, Degussa) can be photodegraded of methyl orange dye.

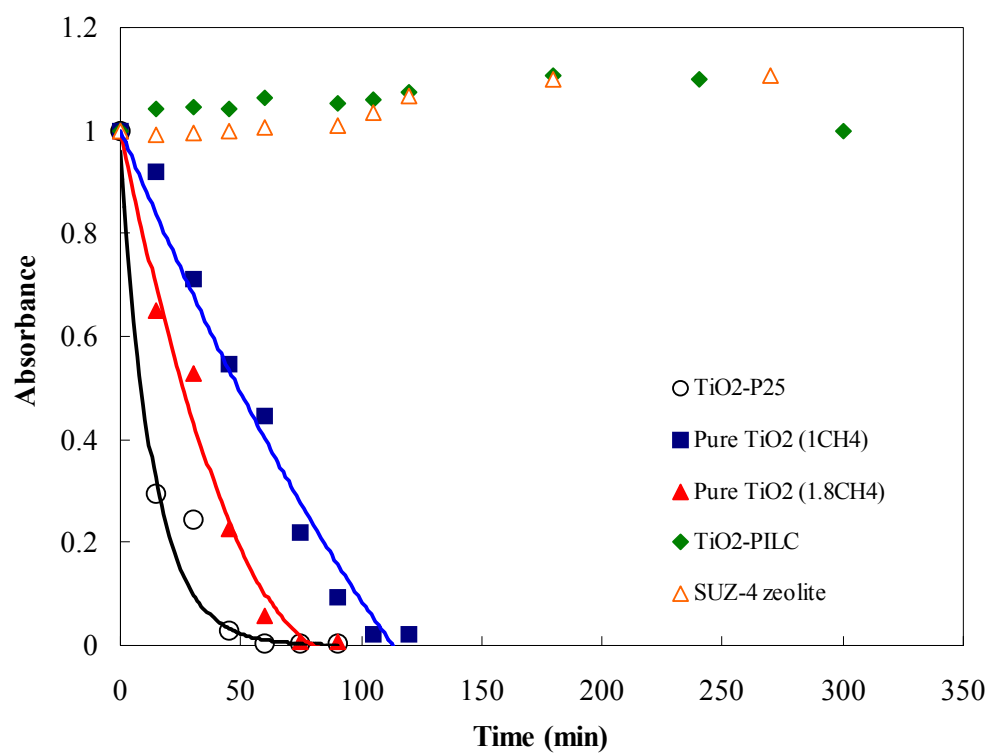


Figure 41 UV-vis absorption intensity at 460 nm for photocatalytic degradation of methyl orange dye of SUZ-4 zeolite, TiO_2 -PILC and TiO_2 .